Revisiting the Mechanism of Dioxygen Activation in Soluble Methane Monooxygenase from M. capsulatus (Bath): Evidence for a Multi-Step Proton-Dependent Reaction Pathway

Citation: Tinberg, Christine E., and Stephen J. Lippard. "Revisiting the Mechanism of Dioxygen Activation in Soluble Methane Monooxygenase from M. capsulatus (Bath): Evidence for a Multi-Step, Proton-Dependent Reaction Pathway." Biochemistry 48, no. 51 (December 29, 2009): 12145-12158.

As Published: http://dx.doi.org/10.1021/bi901672n

Publisher: American Chemical Society (ACS)

Persistent URL: http://hdl.handle.net/1721.1/82145

Version: Author's final manuscript: final author's manuscript post peer review, without publisher's formatting or copy editing

Published in final edited form as:
Biochemistry. 2009 December 29; 48(51): 12145–12158. doi:10.1021/bi901672n.

Revisiting the Mechanism of Dioxygen Activation in Soluble Methane Monooxygenase from *M. capsulatus* (Bath): Evidence for a Multi-Step, Proton-Dependent Reaction Pathway

Christine E. Tinberg[†] and **Stephen J. Lippard**[†,*]
Department of Chemistry, Massachusetts Institute of Technology, Cambridge, MA 02139

Abstract

Stopped-flow kinetic investigations of soluble methane monooxygenase (sMMO) from *M. capsulatus* (Bath) have clarified several discrepancies that exist in the literature regarding aspects of catalysis by this enzyme. The development of thorough kinetic analytical techniques has led to the discovery of two novel oxygenated iron species that accumulate in addition to the well-established intermediates H_{peroxo} and Q. The first intermediate, P^*, is a precursor to H_{peroxo} and was identified when the reaction of reduced MMOH and MMOB with O_2 was carried out in the presence of ≥578 μM methane to suppress the dominating absorbance signal due to Q. The optical properties of P^* are similar to those of H_{peroxo}, with ε_{420} = 3500 M^{-1} cm^{-1} and ε_{720} = 1250 M^{-1} cm^{-1}. These values are suggestive of a peroxo-to-iron(III) charge-transfer transition and resemble those of peroxodiiron(III) intermediates characterized in other carboxylate-bridged diiron proteins and synthetic model complexes. The identified second intermediate, Q^*, forms on the pathway of Q decay when reactions are performed in the absence of hydrocarbon substrate. Q^* does not react with methane and is independent of buffer content. Its optical spectrum displays a unique shoulder at 455 nm. Studies conducted at different pH values reveal that rate constants corresponding to P^* decay/H_{peroxo} formation and H_{peroxo} decay/Q formation are both are significantly retarded at high pH and indicate that both events require proton transfer. The processes exhibit normal kinetic solvent isotope effects (KSIEs) of 2.0 and 1.8, respectively, when the reactions are performed in D_2O. Mechanisms are proposed to account for the observations of these novel intermediates and the observed proton transfer dependencies of P^* decay/H_{peroxo} formation and H_{peroxo} decay/Q formation.

Methane monooxygenases (MMOs[1]) from methanotrophic bacteria catalyze the remarkable oxidation of methane to methanol at ambient temperatures and pressures (1). The type X methanotroph *Methylococcus capsulatus* (Bath), hereafter *Mc*, harbors two functionally convergent MMOs, a copper-containing membrane-bound form (pMMO) and an iron-dependent soluble enzyme (sMMO) that is expressed only at low copper-to-biomass ratios or when the bacteria are grown in a fermentor to high cellular densities (2, 3). Whereas the reaction mechanism of pMMO remains largely elusive due to difficulties in working with a

*To whom correspondence should be addressed. lippard@mit.edu. Telephone: (617) 253-1892. Fax: (617) 258-8150..
†Massachusetts Institute of Technology

Supporting Information Available. Derivation of eqs 2–4 and Figures S1–S12. This material is available free of charge via the Internet at http://pubs.acs.org.

[1]Abbreviations: MMO, methane monooxygenase; pMMO, particulate methane monooxygenase; sMMO, soluble methane monooxygenase; MMOH, hydroxylase component of sMMO; MMOB, regulatory component of sMMO; MMOR, reductase protein of sMMO; H_{peroxo}, peroxodiiron intermediate species in MMOH; Q, di(μ-oxo)diiron(IV) intermediate species of MMOH; P^*, transient H_{peroxo} precursor, Q^*, decay product of Q; MOPS, 3-(N-morpholino)propanesulfonic acid; EXAFS, extended x-ray absorption fine structure; EPR, electron paramagnetic resonance; KSIE, kinetic solvent isotope effect; RNR, ribonucleotide reductase; T4mo, toluene 4-monooxygenase; T4moD, regulatory component of toluene 4-monooxygenase.

membrane protein, that of sMMO has been studied extensively and much is known about the oxidation of methane by this enzyme.

sMMO requires three protein components for efficient catalysis. A dimeric hydroxylase (MMOH) houses two copies of a carboxylate-bridged diiron active site, a reductase (MMOR) acquires electrons from NADH and transfers them to the hydroxylase, and a regulatory protein (MMOB) couples electron consumption to substrate oxidation. The resting state of the hydroxylase (H_{ox}) active site is a di(μ-hydroxo)(μ-carboxylato)diiron(III) species. Upon two-electron reduction to the diferrous state (H_{red}), the bridging hydroxide ligands dissociate and the diiron center reacts rapidly with O_2 in the presence of MMOB. The events that occur as a result of this reaction have been characterized by multiple spectroscopic methods, and a series of oxygenated-iron intermediates accumulate prior to regeneration of the enzyme resting state (4–8).

Early studies relied on Mössbauer spectroscopy to probe the reaction of $MMOH_{red}$ with O_2 (7, 8). The first species observed by this method after addition of O_2 is a peroxodiiron(III) unit comprising two antiferromagnetically coupled iron centers of indistinguishable Mössbauer parameters $\delta = 0.66$ mm/s and $\Delta E_Q = 1.51$ mm/s. UV-vis spectroscopy also supported the formation of a peroxodiiron(III) species as the first observable intermediate, and global analyses of stopped-flow optical data demonstrated optical bands centered around 720 nm ($\varepsilon = 1800\ M^{-1}\ cm^{-1}$) and 420 nm ($\varepsilon = 4000\ M^{-1}\ cm^{-1}$) for this species, assigned as peroxo-to-iron charge transfer transitions (9, 10). The signals arising from Mössbauer and optical spectroscopy were attributed to the same peroxodiiron(III) unit because the decay rates measured by these two methods were identical. This intermediate was termed H_{peroxo}.[2] The formation rates reported by these two methods differed by an order of magnitude, however. The presence of multiple peroxodiiron(III) species with similar Mössbauer parameters but distinct optical signatures was suggested to explain this disparity, although there was no direct evidence for this proposal. The presence of various peroxodiiron(III) species that accumulate on the reaction pathway was later addressed in a study probing the kinetics of O_2 activation in MMOH from *M. trichosporium* OB3b, hereafter referred to as *Mt*, which provided direct evidence for an optically distinct H_{peroxo} precursor, P* (4). Experiments on the *Mc* enzyme provided no such evidence for this species.

Much effort has been devoted to understanding the nature of H_{peroxo}. Attempts to elucidate the binding mode of the peroxo moiety have been unsuccessful and there is no consensus on the structure of this intermediate. Analogy to peroxodiiron(III) species generated in other non-heme diiron enzymes, such as those formed in the W48F/D84E variant of ribonucleotide reductase (RNR) (12, 13), at the ferroxidase center of frog M ferritin (14), in Δ^9-desaturase (15), and in human deoxyhypusine hydroxylase (16), supports a symmetric *cis*-μ-1,2 peroxide binding configuration. Some theoretical studies confirm this assignment (17), whereas others favor a nonplanar $\mu\text{-}\eta^2\text{:}\eta^2$ geometry (18–20). The protonation state of the H_{peroxo} peroxo moiety also remains an unanswered question.

H_{peroxo} oxidizes electron rich substrates such as propylene (10) and diethyl ether (9); however, in the absence of such substrates it rapidly decays to intermediate Q, an antiferromagnetically coupled diiron(IV) unit responsible for methane oxidation. Structural characterization of Q by EXAFS spectroscopy revealed a short Fe-Fe distance of 2.46 Å from which a di(μ-oxo)diiron(IV) "diamond core" was postulated (21). The intense optical bands of Q centered at 350 nm ($\varepsilon = 3600\ M^{-1}\ cm^{-1}$) and 420 nm ($\varepsilon = 7200\ M^{-1}\ cm^{-1}$) that trail into the near infrared ($\varepsilon_{720} \approx 1000\ M^{-1}\ cm^{-1}$) have been used as a handle for mechanistic studies (5–8). Such experiments demonstrated that the decay rate of this

[2] H_{peroxo} is denoted P in studies of sMMO from *M. trichosporium* OB3b.

absorbance feature is accelerated in the presence of methane and other substrates (4, 6, 7, 10, 11), suggesting that intermediate Q is responsible for oxidation chemistry. The mechanism of substrate oxidation by Q been the subject of many investigations (11, 22, 23), and it is generally believed that these processes occur by two single electron transfer events from substrate to Q, generating a transient bound radical species (24). In the absence of substrate, Q decays slowly to H_{ox} by an unknown pathway that requires the acquisition of two electrons and two protons at the diiron center. The mechanism by which this process occurs has not received much, if any, attention in the literature.

Another enigmatic aspect of MMOH catalysis is the mechanism of H_{peroxo} to Q conversion with concomitant O–O bond cleavage. Two distinct mechanisms have been proposed for this transformation based on existing inorganic chemistry (Scheme 1). The first involves homolytic O–O bond scission and concerted rearrangement of an H_{peroxo} μ-η^2:η^2 core to form intermediate Q in a manner similar established peroxodicopper(II) transformations (25, 26). The second includes proton-promoted heterolytic O–O bond cleavage and rearrangement of the diiron center, a mechanism analogous to the generally accepted route of O–O bond scission in cytochromes P450 (27, 28). Key differences between these two proposed mechanisms are the origin of the two bridging oxygen atoms of Q and the proton requirement for the O–O bond-breaking process. Spectroscopic studies to ascertain whether one or both of the oxygen atoms derived from $^{18}O_2$ are incorporated into Q have been unsuccessful to date.

Kinetic investigations of the proton requirement of H_{peroxo}-to-Q conversion gave contradictory results in the *Mc* and *Mt* enzymes. The rate constants associated with H_{peroxo} formation and H_{peroxo} decay/Q formation in *Mt* MMOH are pH-dependent and display normal solvent kinetic isotope effects (KSIE) in proton inventory studies, results that implicated rate-limiting transfer of a single proton in both steps (29). The slopes of the proton inventory plots led the authors to conclude that H_{peroxo} formation and its subsequent conversion to Q include the addition of two protons to an iron-bound peroxide oxygen atom followed by heterolytic O–O bond scission coupled to release of a H_2O molecule. However, studies of MMO from *Mc* found that these processes were neither pH-dependent nor exhibited KSIEs greater than unity, consistent with proton transfer not being rate-limiting in either of these steps (7). A reconciliation of these results is important for understanding the H_{peroxo}-to-Q pathway and O–O bond cleavage mechanism in this enzyme, elucidating the protonation state and structure of H_{peroxo}, and guiding experiments to devise synthetic models for the reaction chemistry.

Although these studies provide a framework for understanding O_2 activation for attack on the strong and kinetically difficult to access C–H bond of methane, many aspects of MMOH catalysis remain vague. To clarify some of the ambiguities, we have in the present study employed stopped-flow optical spectroscopy to reexamine the mechanism of dioxygen activation in MMOH from *Mc* Our findings provide direct evidence for a multi-step reaction pathway in which a minimum of four oxygenated-iron intermediates accumulate, including P^* previously identified in the *Mt* enzyme as well as a novel species termed Q^*. Q^* forms as a result of Q decay, is not reactive toward methane, and is most likely derived from Q. Comparison of these results to previous work reveals that the H_{peroxo} species previously characterized by optical and Mössbauer spectroscopy are two distinct peroxodiiron(III) intermediates rather than one single entity. Additionally, in contrast with previous reports from this enzyme, our data show that H_{peroxo} formation and H_{peroxo} decay/Q formation are both pH-dependent and exhibit normal KIEs, as found for the *Mt* MMOH. The results indicate that both processes involve rate-limiting proton transfer steps, and possible mechanisms to explain these results are discussed.

MATERIALS AND METHODS

General Considerations

Hydroxylase protein (MMOH) was purified from *Methylococcus capsulatus* (Bath) as previously described, except that a Q Sepharose fast flow anion exchange column (4 × 50 cm) was used in place of the final MonoQ column. Protein obtained by this procedure typically exhibited specific activities of 400–500 mU/mg for propylene oxidation at 45 °C and iron contents of 4.0 ± 0.2 iron atoms per protein dimer (9, 10). The regulatory (MMOB) and reductase (MMOR) proteins were expressed recombinantly in *E. coli* and purified by established methods (30, 31). The buffer system employed in all experiments was 25 mM potassium phosphate (6.6 ≤ pH ≤ 8.6), prepared by adding the appropriate volumes of 1 M K_2HPO_4 and 1 M KH_2PO_4 to ddH_2O and adjusting the pH using HCl or NaOH. Distilled water was deionized with a MilliQ filtering system. Methane (99.9%) was purchased from Airgas (Independence, OH). All other chemicals were obtained from Aldrich and used as received.

Stopped-Flow Optical Spectroscopy

Single turnover transient kinetic experiments were performed on a Hi-Tech Scientific (Salisbury, UK) SF-61 DX stopped-flow spectrophotomer made anaerobic by flushing the flow circuit extensively with ~10 mM $Na_2S_2O_4$ and then N_2-purged buffer. A protein solution containing $MMOH_{red}$ and 2 equiv of MMOB was prepared by reduction with $Na_2S_2O_4$ in the presence of methyl viologen, as described previously except that 25 mM potassium phosphate buffer was used instead of MOPS (10). Excess reducing agent was removed by dialyzing the mixture twice against 500 mL buffer for ~1 hr each. Following dialysis, the protein was transferred to the anaerobic stopped-flow instrument in a glass tonometer.

For stopped-flow experiments performed in the absence of substrate, reduced protein solution was mixed rapidly with an equivalent volume of O_2-saturated buffer of the appropriate pH. For experiments performed in the presence of substrate, the reduced protein solution was mixed with buffer containing CH_4 and O_2. Double-mixing stopped-flow (DX-SF) experiments were performed by injecting a solution of substrate-containing buffer at the time of maximization of the intermediate of interest. Substrate-containing solutions were prepared by drawing the appropriate volumes of O_2- and CH_4-saturated buffers into a 10 mL gastight Hamilton syringe. Approximate methane and dioxygen concentrations were calculated using the solubility constants of gaseous CH_4 and O_2 in water at 20 °C, the temperature at which the solutions were prepared (1.54 mM for CH_4 and 1.39 mM for O_2) (32).

Q photodecomposes in response to the Xe lamp of the diode array apparatus (10); therefore, reactions investigating Q and events resulting from Q decay were all collected at single wavelengths using the photomultiplier tube, limiting the number of data points that could be obtained. Data were collected using Kinetic Studios (Hi-Tech Scientific) and fit with KaleidaGraph v 3.6 (Synergy Software) and Origin v 6.1 (OriginLab Corporation). All experiments were performed at 4 °C. The concentration of MMOH in the optical cell after mixing was 50 μM in all experiments unless otherwise noted. All experiments were carried out at least in triplicate using at least three different batches of proteins.

KSIE Measurements

Deuterium oxide (99.9%) was purchased from Cambridge Isotope Laboratories (Andover, MA). Buffers containing 25 mM potassium phosphate (pD 7.0) were prepared by adding weighted mixtures of K_2HPO_4 and KH_2PO_4 to the appropriate amount of D_2O. The pD of

the buffer was adjusted with DCl, where pD = "pH meter reading" + 0.4. MMOH and MMOB were individually exchanged into D_2O buffer by three repeated rounds of concentration and dilution in Amicon centrifugal concentrators (Millipore, Billerica, MA) over the course of four hr, which was found to be sufficient. Protein solutions were prepared and reduced as noted above, except that dialyses were carried out in D_2O buffer for ~1.5 hr each. All KSIE experiments were performed at 5 °C. Adequate comparisons to data collected in H_2O at 4 °C could be made because the one degree temperature difference was found to have a negligible effect on the rate constants. Approximate methane concentrations for these experiments were calculated using the solubility constant of CH_4 in D_2O at 20 °C (1.64 mM) (32).

Data Analysis

Except where noted, all experiments were performed under first-order or pseudo-first order conditions and were analyzed accordingly. Multiple chemically reasonable kinetic models were considered when analyzing the results of stopped-flow studies probing the reactions of $MMOH_{red}$:2B with O_2 and O_2/CH_4 mixtures. The kinetic solutions reported here are those that required the minimal number of variable parameters to adequately fit the data. Data fits were evaluated by examining the magnitude of the difference between the fit and the data at every data point collected (residual plots) and were accepted or rejected on the basis of these fit residuals, the reduced chi-squared value describing the goodness-of-fit ($\chi^2_{red} = \chi^2/$ degrees of freedom), and the parameter dependencies.

RESULTS

$MMOH_{red}$:2B + O_2: Reactions in the Presence of Methane

The results of numerous studies provide compelling evidence that intermediate Q is the oxygenated iron species responsible for methane oxidation. It is generally accepted that H_{peroxo} does not react with this substrate. To reinvestigate H_{peroxo} formation and decay, and identify other optically significant events that occur prior to formation of Q, we reasoned that the dominant optical signal of Q will be suppressed if sufficiently high concentrations of this substrate are present such that the rate of Q decay becomes much faster than that of its formation. Under these conditions, the weaker optical signatures of preceeding intermediates can be uncovered and evaluated by kinetic methods. Stopped-flow optical spectroscopy was therefore employed to monitor the optical changes that occur at 420 nm upon mixing $MMOH_{red}$ and 2 equiv MMOB with a solution containing O_2 and CH_4 (Fig. 1). At low methane concentrations (< 578 μM), the optical signal changes with increasing substrate concentration, suggesting that the Q decay rate is not sufficiently fast to prevent accumulation of this intermediate. However, at methane concentrations ≥ 578 μM, the optical signal no longer changes with increasing substrate concentration, indicating that Q does not accumulate under these conditions, presumably because of rapid reaction with the substrate. Although the optical signal of Q is fully suppressed when $[CH_4] \geq 578$ μM, a time-dependent rise and decay in absorbance at 420 nm is observed, indicating the presence of at least one intermediate that is unaffected by the presence of methane and that absorbs at this wavelength (Fig. 1). Because H_{peroxo} absorbs at 420 nm (9, 10), it is reasonable to assume that this intermediate contributes to some of or all of the observed signal.

To investigate the processes associated with the rise and decay in absorbance observed at $[CH_4] \geq 578$ μM and determine whether it is solely due to absorbance by H_{peroxo}, data collected under these conditions at 420 nm and 720 nm were fit by using non-linear least squares methodology. Previous studies probing reactions of $MMOH_{red}$:2B with O_2 have generally relied on fitting single-wavelength data to obtain kinetic information about the processes that occur as a result of this reaction. Here, we found that fitting single-

wavelength data sets to sums of exponentials or analytical kinetic models often resulted in solutions that appeared satisfactory for the data being analyzed but were poor descriptors of data collected under the same conditions at different wavelengths. By fitting data collected at only a single wavelength it was therefore easy to converge upon an incorrect solution. A more reliable method of fitting the kinetic traces was afforded by collecting data at a minimum of two wavelengths and simultaneously fitting these data sets using shared rate constant parameters (33). This approach reduces the number of parameters to be fit by adding constraints to the data and therefore increases our confidence that the model used to fit the data is correct if a satisfactory result is obtained.

Using this method, we observed that the rise and decay in absorption in the presence of high concentrations of methane did not fit well to a sum of two exponentials describing the process $H_{red} \rightarrow H_{peroxo} \rightarrow H_{ox}$ described previously for *Mc* experiments conducted in the presence of methane (10). Instead, the data fit well to a sum of three exponentials representing a minimum of three processes, as reported for the *Mt* system (4). Two of those processes must arise from H_{peroxo} formation and from H_{peroxo} decay. The additional feature observed in the data suggests one of the three following possibilities: (i) accumulation of an additional transient species on the reaction pathway, (ii) two productive populations of H_{red} which proceed with different rates constants to the H_{peroxo} intermediate upon reaction with O_2, or (iii) two pathways that lead to H_{peroxo} decomposition with different rate constants. Although process i seems most likely, processes ii and iii could arise from a heterogeneous population of MMOH/MMOB complexes (6) or via a half-sites reactivity mechanism in which the two diiron sites in the hydroxylase react with O_2 on different timescales (34). Possibility (iii) was rejected when truncation of the data to include only points following maximal absorbance accumulation fit well to a single exponential decay process. Furthermore, the amplitude describing the additional phase is positive in the exponential fit, suggesting that it contributes to the rise phase of the absorbance profile.

Possibilities (i) and (ii) were assessed by fitting the data to differential equations 1 and 2 describing the analytical solutions to models i and ii in Scheme 2. H_{peroxo} presumably decays to Q under these conditions; however, because Q is depleted faster than it forms it does not accumulate and therefore does not have to be accounted for in the kinetic model. Fitting the data to Scheme 2i, which includes an

$$Abs_{\lambda}(t) = [H_{red}]_0 \left\{ \begin{array}{l} \varepsilon_{H_{ox}} + \left(\varepsilon_{H_{red}} - \varepsilon_{H_{ox}}\right)\left(e^{-k_1' t}\right) + \left(\left(\varepsilon_{P^*} - \varepsilon_{H_{ox}}\right)\left(\frac{k_1'}{k_2 - k_1'}\right)\left(e^{-k_1'} - e^{-k_2 t}\right)\right) + \\ \left(\left(\varepsilon_{H_{peroxo}} - \varepsilon_{H_{ox}}\right)\left(\frac{k_1' k_2}{k_2 - k_1'}\right)\left\{\left(\frac{1}{k_3 - k_1'}\right)\left(e^{-k_1' t} - e^{-k_3 t}\right) - \left(\frac{1}{k_3 - k_2}\right)\left(e^{-k_2 t} - e^{-k_3 t}\right)\right\}\right) \end{array} \right\} \quad (1)$$

$$\begin{aligned} \mathrm{Abs}_{\lambda}(t) = {} & \varepsilon_{H_{ox}}\left([H_{red1}]_0 + [H_{red2}]_0\right) + \left(\varepsilon_{H_{red}} - \varepsilon_{H_{ox}}\right)[H_{red1}]_0 e^{-k_1' t} + \left(\varepsilon_{H_{red}} - \varepsilon_{H_{ox}}\right)[H_{red2}]_0 e^{-k_2' t} \\ & + \left(\varepsilon_{H_{peroxo}} - \varepsilon_{H_{ox}}\right)\left(k_1'[H_{red1}]_0\left(\frac{1}{k_3 - k_1'}\right)\left(e^{-k_1' t} - e^{-k_3 t}\right) + k_2'[H_{red2}]_0\left(\frac{1}{k_3 - k_2'}\right)\left(e^{-k_2' t} - e^{-k_3 t}\right)\right) \end{aligned} \quad (2)$$

additional intermediate that proceeds H_{peroxo} formation, P*, afforded excellent results with $k_1' = 6.7 \pm 0.9\ s^{-1}$, $k_2 = 0.75 \pm 0.04\ s^{-1}$, $k_3 = 0.34 \pm 0.03\ s^{-1}$ (Fig. 2). The values of k_2 and k_3 measured in this work are the same as those reported for H_{peroxo} formation and decay by optical spectroscopy in MOPS buffer (9, 10). We have therefore assigned the second species as H_{peroxo} and the precursor that forms in the faster phase governed by k_1' as the novel transient P*. In contrast, fits to model ii, which yielded similar rate constants, were not as satisfactory (Fig. S1, Supporting Information). The best fit from this model resulted when H_{red} contributed 20% of a rapidly reacting diiron population and 80% of a slowly reacting population, which is inconsistent with a half-sites reactivity mechanism. The fits obtained from this model demonstrated unacceptably large parameter error values and a worse χ^2_{red}

value than that obtained from process i. Also, the residual plots from these fits demonstrated sinusoidal behavior indicative of incorrect kinetic modeling. Therefore, both the goodness-of-fit parameters and fit residuals indicate that the $H_{red} \rightarrow P^* \rightarrow H_{peroxo} \rightarrow H_{ox}$ model is more appropriate.

Kinetic Characterization of P*

Data collected at 420 nm and 720 nm in the presence of 578 μM CH_4 were fit simultaneously to eq 1 by sharing rate constant parameters and setting $[H_{red}]_0$ to 32 μM to account for the observation that only 32% of the 100 μM diiron sites in the sample proceed though a productive pathway (7). The approximate extinction coefficients obtained were $\varepsilon_{420} \approx 3500\ M^{-1}\ cm^{-1}$ and $\varepsilon_{720} \approx 1250\ M^{-1}\ cm^{-1}$ for P* and $\varepsilon_{420} \approx 3880\ M^{-1}\ cm^{-1}$ and $\varepsilon_{720} \approx 1350\ M^{-1}\ cm^{-1}$ for H_{peroxo}, although these numbers are probably underestimated because the protein preparations used in these studies display significantly higher steady state activities than those previously employed to measure the percentage of active diiron sites. The similarities between the optical parameters of P* and H_{peroxo} reveal that the two intermediates are electronically similar. The dependencies of k_1' on O_2 concentration were measured to probe the mechanism of P* formation. No change was observed for k_1' or the rate constants governing the subsequent steps when the concentration of O_2 was varied in the experiments and the data were fit to eq 1, indicating that the first irreversible step in the reaction proceeds P* formation (Fig. S2).

$MMOH_{red}$:2B + O_2: Reactions in the Absence of Methane

Reactions of reduced MMOH:2B with O_2 were monitored to study the events that occur when methane is not present. Previous experiments conducted in MOPS buffer indicated that the data should fit well to an analytical model describing the process $H_{red} \rightarrow H_{peroxo} \rightarrow Q \rightarrow H_{ox}$ (9); however, data collected at 420 nm and 720 nm did not fit well to this solution (Fig. S3) or to a sum of three exponentials describing the three processes involved in this model. Instead, the data fit well to a sum of four exponentials describing a minimum of four processes. The values of the two fastest rate constants obtained from these fits are the same as those of the rate constants describing H_{peroxo} formation (k_2) and decay (k_3) in experiments performed in the presence of high methane concentrations (vide supra), allowing us to unambiguously assign these events.[3]

To correlate the two slower observables with enzymatic events, two different chemically reasonable models were considered, and fits of the data to differential equation solutions for these models were compared. The first model describes a process in which a colored intermediate that follows Q decay (denoted Q*) contributes to the observed optical events (iii, Scheme 3). The second model describes a situation in which there are two populations of Q that decay on different timescales (iv, Scheme 3). Fits of the data to eqs. 3 and 4, the respective differential solutions to models iii and iv, are shown in

[3]The first process $H_{red} \rightarrow P^*$ does not have to be accounted for in these analyses because a significant portion of the rise in absorbance associated with this transformation occurs during the dead time of the stopped-flow instrument and because the process is characterized by only a very modest change in absorbance relative to events that follow. Including an additional term from the first process $H_{red} \rightarrow P^*$ did not reduce the χ^2_{red} of the fit, and the parameter dependency of the rate constant associated with that process was close to unity, suggesting that the inclusion of this step is unnecessary. One assumption implicit in these analyses is that $[P^*] = 0$ at t = 0 s. Such is not the case; however, the excellent fits obtained using this model and the fact that the fastest rate constant obtained from these fits matches that of k_2 measured in experiments performed in the presence of 578 μM CH_4 justify the approximation.

$$\mathrm{Abs}_{\lambda}(t) = \left\{ \begin{array}{l} \varepsilon_{H_{ox}}[P^*]_0 + \left(\varepsilon_{P^*} - \varepsilon_{H_{ox}}\right)\left([P^*]_0 e^{-k_2 t}\right) + \left(\varepsilon_{H_{peroxo}} - \varepsilon_{H_{ox}}\right)\left([P^*]_0 \left(\frac{k_2}{k_3 - k_2}\right)\left(e^{-k_2 t} - e^{-k_3 t}\right)\right) + \\ \left(\varepsilon_{Q} - \varepsilon_{H_{ox}}\right)\left(k_3[P^*]_0 \left(\frac{k_2}{k_3 - k_2}\right)\left\{\left(\frac{1}{k_4 - k_2}\right)\left(e^{-k_2 t} - e^{-k_4 t}\right) - \left(\frac{1}{k_4 - k_3}\right)\left(e^{-k_3 t} - e^{-k_4 t}\right)\right\}\right) + \\ \left(\varepsilon_{Q^*} - \varepsilon_{H_{ox}}\right)\left(k_4 k_3[P^*]_0 \left(\frac{k_2}{k_3 - k_2}\right)\left\{ \begin{array}{l} \left(\frac{1}{k_4 - k_2}\right)\left(\frac{1}{k_5 - k_2}\right)\left(e^{-k_2 t} - e^{-k_5 t}\right) - \left(\frac{1}{k_4 - k_2}\right)\left(\frac{1}{k_5 - k_4}\right)\left(e^{-k_4 t} - e^{-k_5 t}\right) - \\ \left(\frac{1}{k_4 - k_3}\right)\left(\frac{1}{k_5 - k_3}\right)\left(e^{-k_3 t} - e^{-k_5 t}\right) + \left(\frac{1}{k_4 - k_3}\right)\left(\frac{1}{k_5 - k_4}\right)\left(e^{-k_4 t} - e^{-k_5 t}\right) \end{array} \right\}\right) \end{array} \right\} \quad (3)$$

$$\mathrm{Abs}_{\lambda}(t) = [P^*]_0 \left(\begin{array}{l} \varepsilon_{P^*} + \left(\varepsilon_{P^*} - \varepsilon_{H_{ox}}\right)e^{-k_2 t} + \left(\varepsilon_{H_{peroxo}} - \varepsilon_{H_{ox}}\right)\left(\frac{k_2}{k_3 - k_2}\right)\left(e^{-k_2 t} - e^{-k_3 t}\right) + \\ \left(\varepsilon_{Q} + \varepsilon_{H_{ox}}\right)\left(\frac{k_3 k_2}{k_3 - k_2}\right)\left(\left(\frac{1}{k_4 + k_5 - k_2}\right)\left(e^{-k_2 t} - e^{-(k_4 + k_5)t}\right) - \left(\frac{1}{k_4 + k_5 - k_3}\right)\left(e^{-k_3 t} - e^{-(k_4 + k_5)t}\right)\right) \end{array} \right) \quad (4)$$

Fig. 3 and Fig. S4. Fits of the data to model iii afforded excellent results, with k_2 = 0.75 ± 0.05 s^{-1}, k_3 = 0.37 ± 0.01 s^{-1}, k_4 = 0.011 ± 0.002 s^{-1}, and k_5 = 0.0026 ± 0.0001 s^{-1}, whereas those to iv yielded poor fits with sinusoidal residual plots and large parameter dependencies (~1). χ^2_{red} values for fits to iii were more than order of magnitude better than those to iv, allowing us to unambiguously confirm iii as the process with the minimum number of steps necessary to describe the data. Global analysis of kinetic data collected at various wavelengths using a diode array detector was employed to approximate the absorption spectrum of Q*. Although spectral determination by this method can be biased by the absorbance of other species present during the reaction, it has been used widely to estimate the optical and fluorescent properties of individual components in complex mixtures (33). The optical spectrum of Q* obtained by this method displays a band centered around 420 nm and a shoulder around 455 nm that is not present in the optical spectrum of Q (Fig. 4).

Double-Mixing Stopped Flow Optical Spectroscopy: Q/Q* + CH_4

To address the relative significance of Q and Q* with respect to enzyme function, double mixing stopped-flow experiments were conducted in which either intermediate was generated and then mixed with a solution containing 770 μM CH_4. For each experiment, appropriate age times between the first and second push needed to monitor reactions of Q and Q* were determined by preparing a speciation plot using rate constants extracted from fits of the data to model iii (vide supra) and identifying the t_{max} of the two intermediates. From this method, t_{max} values for Q and Q* were 13 s and 186 s, respectively (Fig. 5).

Data investigating reactions of Q with CH_4 at 420 nm were fit well by a single exponential decay process having k = 3.9 ± 0.2 s^{-1} (Fig. S5). This rate constant is ~350 times larger than that for Q decay identified in single-mixing experiments (vide supra) and that measured in double-mixing control experiments in which the intermediate was accumulated and mixed with buffer instead of CH_4 (k_3 = 0.010 s^{-1}). The acceleration of Q decay in the presence of CH_4 and the fact a term for Q* was not necessary to fit the data indicate that Q is depleted by a different pathway in the presence of methane than in the absence. The mechanism of methane-promoted Q decay most likely arises from rapid reaction with this substrate (4, 10).

Experiments probing reactions of Q* with CH_4 at 420 nm revealed the presence of two distinct decay processes (Fig. S5). Because these two phases are separated by several orders of magnitude in rate constant and are independent of each other (vide infra), the data were fit well by separately analyzing each event. The rate constants for the two phases obtained by this method were 3.6 ± 0.2 s^{-1} and 0.002 ± 0.001 s^{-1}. The observation that the faster rate constant agrees with that of methane-promoted Q decay (vide supra) allows us to unambiguously assign this process. Indeed, at the age time employed in these experiments (186 s), the protein sample is a complex mixture of 19% Q, 60% Q*, and 21% H_{ox} (Fig. 5). It is therefore necessary to include a term for the substantial population of Q present,

because this intermediate absorbs significantly at the wavelength employed (ε_{420} = 8415 M^{-1} cm^{-1}). The rate constant describing the slower event is identical to that of Q^* decay measured in single-mixing experiments (vide supra) as well as that monitored in double-mixing control experiments (k_3 = 0.0028 s^{-1}). These results indicates that this process represents Q^* decay and that its decay rate is not altered by the presence of methane. These results demonstrate that Q is competent for methane oxidation and that Q^* does not react with this substrate. These conclusions are summarized in Scheme 4.

Effect of Buffer on Q Decay

The data strongly suggest the presence of a novel intermediate Q^* that forms as Q decays. To confirm that Q^* is on the reaction pathway and not a physiological irrelevant adduct of Q formed by reaction with buffer, the experiments were repeated in 25 mM sodium cacodylate, pH 7.0 (Fig. S6) and in 25 mM MOPS, pH 7.0 (Fig. S7). Attempts to fit the data to a three exponential process were unsuccessful and the data could only be well fit when a fourth exponential was included. The data fit nicely to the $P^* \rightarrow H_{peroxo} \rightarrow Q \rightarrow Q^* \rightarrow H_{ox}$ model (eq 3), and the rate constants obtained from the fits were within error of those measured in phosphate buffer. The exception is k_3, the value of which was reduced to 0.21 s^{-1} in cacodylate buffer. This reduction might reflect a steric constraint imposed by large cacodylate molecules on this transformation, which involves geometric reorganization at the diiron center. The necessity of including a term for Q^* in these fits indicates that this phenomenon is general and not specific to the buffer system employed. Double-mixing stopped-flow experiments conducted to determine whether Q reacts with MOPS demonstrated that this intermediate does indeed oxidize this organic molecule, but at a very slow rate of 0.074 M^{-1} s^{-1}. This reaction is so slow that it does not significantly affect the kinetics of the single-mixing experiments performed in 25 mM MOPS (Fig. S8). The results of these studies demonstrate that all events are independent of buffer content and are therefore properties of the protein itself rather than physiologically irrelevant buffer-protein adducts.

Proton Requirements of $MMOH_{red}$:2B + O_2 Reactions

Reactions of $MMOH_{red}$:2B with O_2 were monitored in the absence and presence of 578 μM methane at different pH values in the range 6.6 – 8.6. The enzyme system is stable over the duration of the experiments at room temperature for all pH values monitored. The data clearly demonstrate that the external buffer pH affects the kinetics of the oxygenated iron intermediates that accumulate (Fig. 6). For example, data collected in the absence of methane display time-dependent rise and decay phases at 420 nm when pH < 8.6; however, as the buffer pH is increased, the kinetics of the processes contributing to these features are altered such that the amplitude of the signal is reduced. At pH 8.6, rise and decay processes are no longer observed, indicating that colored intermediates no longer build up under these conditions, either because the kinetics are altered such that they no longer favor accumulation of these species or because the transients do not form under these conditions.

To determine which steps are altered, data collected at 420 nm and 720 n were fit simultaneously at different pH values. Data from reactions probing the $MMOH_{red}$:2B + O_2 reaction in the presence of methane fit well to eq 1 describing Scheme 2i at all pH values employed. Experiments in the absence of methane were analyzed satisfactorily with eq 3, the solution to Scheme 3iii.[4] Using these fitting procedures, k_2 and k_3 were found to vary with pH whereas k_1', k_4, and k_5 did not (Fig. 7 and S9). The values of k_2 and k_3 both decrease with increasing pH, suggesting that steps associated with these rate constants are facilitated by or dependent on proton(s). k_2 and k_3 display sigmoidal dependencies on pH, although the experimentally accessible pH range hindered our ability to collect data points near the extrema of each curve where the rate constants flatten out with pH.

The pH titration data for P* decay/ H_{peroxo} formation (k_2) fit well to eq 5 derived from Scheme 5a, which describes a single, reversible ionization event followed by irreversible conversion of the protonated

$$k = \frac{k_{HA}\,10^{(pK_a - pH)}}{1 + 10^{(pK_a - pH)}} + k_A \quad (5)$$

species to H_{peroxo} (Fig. 7a), where k_{HA} and k_A are the rate constants of conversion to H_{peroxo} for the protonated and deprotonated species, respectively (35). A fit of the data to this model afforded k_{HA} = 1.35 s^{-1}, k = 0.08 s^{-1}, and pK_a = 7.2. The small magnitude of k_A and the fact that this number is probably overestimated by our inability to obtain data points at higher pH values strongly suggest that the system does not proceed to H_{peroxo} in the absence of this crucial rate-determining proton transfer step.

The pH titration data for H_{peroxo} decay/Q formation (k_3) fit poorly to eq 5 (Fig. S10), with χ^2_{red} = 0.0021, and were much better approximated by eq 6 derived from Scheme 5b, which describes a doublyionizing

$$k = \frac{k_{H_2A}[H^+]^2 + K_1 k_{HA}[H^+] + k_A K_1 K_2}{K_1 K_2 + K_1[H^+] + [H^+]^2} \quad (6)$$

system (Fig. 7b), where k_{H2A}, k_{HA} and k_A are rate constants for conversion of the doubly protonated, singly protonated, and unprotonated species, respectively, K_1 and K_2 are the acid dissociation constants for the first and second protonation events, and pK_a = −log(K_a) and pH = −log([H]$^+$) (35). A fit of the data to this model afforded k_{H2A} = 0.41 s^{-1}, k_{HA} = 0.19 s^{-1}, k_A = 0.008 s^{-1}, pK_1 = 7.9, and pK_2 = 7.0. χ^2_{red} for the fit was 0.00028, which is an order of magnitude better than that of the fit to eq 5. These data demonstrate that both the monoprotonated and the diprotonated species are able to generate Q, but the unprotonated form cannot. Additionally, the rate of conversion of the diprotonated species is approximately twice as fast as that of the monoprotonated species.

Reactions of $MMOH_{red}$:2B + O_2 in the absence and presence of methane were also conducted in buffer prepared in D_2O to discern the requirement of solvent-derived protons during the processes monitored. Data were fit well in the manner described for reactions of $MMOH_{red}$:2B with O_2 in the absence and presence of CH_4, delivering k_1' = 6.5 ± 2.2 s^{-1}, k_2 = 0.38 ± 0.04 s^{-1}, k_3 = 0.20 ± 0.03 s^{-1}, k_4 = 0.013 ± 0.005 s^{-1}, and k_5 = 0.0024 ± 0.0007 s^{-1} (Fig. S11). The processes governed by k_2 and k_3 therefore display normal kinetic solvent isotope effects (KSIEs) k_H/k_D of 2.0 ± 0.2 and 1.8 ± 0.3, respectively, whereas those of k_1', k_4, and k_5 were not affected by isotopic substitution within the error limits of the experiments. The KSIE magnitudes for k_2 and k_3 are typical for proton transfer reactions (36).

A concern in devising KSIE experiments is that D_2O is slightly more viscous that H_2O, which can lead to data misinterpretation if not properly accounted for. However, the changes of k_2 and k_3 in response to solvent content monitored here are not likely to arise from the increased viscosity effects. Glycerol has affects the single turnover kinetics of this enzyme,

[4]Data collected in the absence of CH_4 at pH 8.2 fit well to a sum of three exponentials instead of the four describing the P* → H_{peroxo} → Q → Q* → H_{ox} process required to fit data collected at the other pH values studied. At pH 8.2 the value of k_3 approaches that of k_4 such that Q does not accumulate to a significant amount and the process does not need to be accounted for. For these fits, the P* → H_{peroxo} → Q → Q* → H_{ox} model was employed but k_4 was fixed at 0.0114 s^{-1}, the average value of this pH-independent rate constant across all pH values employed as this rate constant is pH independent. Acceptable fits were obtained by this method.

but concentrations of this viscogen that mimic viscosity change of D_2O is insufficient to reproduce the measured KSIE (29, 37).

DISCUSSION

The extraordinary ability of methane monooxygenases to catalyze the oxidation of methane selectively to methanol using atmospheric dioxygen has attracted much interest. While experiments probing the mechanism of this transformation have led to the identification of several oxygenated iron intermediate species that are capable of C–H bond abstraction, there are still many questions that remain about events that occur leading up to substrate oxidation and regeneration of the enzyme resting state. In this study, we employed stopped-flow optical spectroscopy to gain insight into the kinetics of the reactions of $MMOH_{red}$ with O_2 in the presence of regulatory protein MMOB.

Origin of Proton Requirement

Previous kinetic experiments performed in our laboratory suggested that none of the transient events initiated by reaction of $MMOH_{red}$:2B with O_2 are pH-dependent nor exhibit significant KSIEs (7). For the pH-dependence studies, these experiments were performed via pH jump methods in which reduced protein in 10 mM MOPS pH 7.0 was mixed rapidly with O_2-saturated 100 mM MOPS at the desired pH. However, if reaction with O_2 and subsequent steps are faster than the pH equilibration of active site residues, then these effects would not have been detected using this method. For studies performed in D_2O, the values of the KSIEs are small (≤ 2) and were most likely overlooked.

The data presented here support those reported for the *Mt* enzyme (29); however, there are some key differences between the results of the two studies. Both investigations find that the pH dependence of P^* decay/H_{peroxo} formation fit well to a model consisting of reversible protonation followed by an irreversible step (Scheme 5a). Studies from the *Mt* enzyme showed that the pH dependence of the H_{peroxo} to Q conversion also fit nicely to this model, but the results reported here clearly demonstrate the model does not adequately represent the data. For the *Mc* enzyme, a model that describes two reversible stepwise protonation events fits the data much better. It seems unlikely that the same intermediate from two closely related sMMO systems require separate mechanisms for proton transfer; however, the origin of the differences is unknown.

The demonstration that P^* decay/H_{peroxo} formation (k_2) and H_{peroxo} decay/Q formation (k_3) are pH dependent and display normal KSIEs around 2 indicate that proton transfer is involved in the rate-determining steps of these processes. Although these results verify the necessity of proton transfer for these steps, they cannot definitively describe the location or mechanism of the events. Translocation of protons could occur at or near the active site or as a result of redox-dependent conformational changes and/or remodeling of protein-protein interactions that alter hydrogen-bonding patterns and accompany structural and electronic changes at the diiron center.

We favor mechanisms for both P^* decay/H_{peroxo} formation and H_{peroxo} decay/Q formation in which transfer of protons occurs at or near the diiron active site or as a result of very minor structural perturbations instead of large ones. It is likely that large conformational changes or protein interactions would result in the formation and breakage of many hydrogen bonds rather than involve direct transfer of one or two protons, as the data indicate. Indeed, structural studies on the hydroxylase from the toluene 4-monooxygenase (T4mo) system demonstrated that >20 new hydrogen bonds form as a result of conformational changes initiated by binding of its regulatory protein T4moD (38).

Additionally, the observed KSIEs of ~ 2.0 are suggestive of direct proton transfer reactions rather than formation of hydrogen bonds, which usually display small, inverse KSIEs (39).

Given these observations, the pH dependencies of k_2 and k_3 are likely to result from proton transfer that occurs at or near the diiron center or from conformational changes restricted to single amino acid side chains that result in direct translocation of protons. However, one consideration that must be taken into account when postulating a mechanism of proton transfer at the MMOH active site is that this cavity is largely hydrophobic and a very large thermodynamic driving force would be necessary to deliver a proton and screen the charges that would be generated during the transfer of that proton. Indeed, this logic is the mainstay of theoretical work that favors the homolytic O–O bond cleavage process of Scheme 1a rather than the heterolytic one of 1b (17, 20, 40). Given this strong motivation to maintain a charge-neutral environment, we propose several possibilities for proton donors and acceptors in the P^* to H_{peroxo} and H_{peroxo} to Q conversion processes.

Proton Donors

The hydrophobic environment of the active site cavity across the entire MMOH subfamily reveals few amino acids typically thought to participate in general acid-base catalysis located within reasonable proton-donating distance to the iron center. Of those that could potentially participate in such reactions, the only candidates are T213, C151, Q140, D143, and D242. With the exception of cysteine and aspartate in a few limiting examples, none of these amino acids typically participate in proton transfer reactions or display pK_a values near the neutral values measured for k_2 and k_3. C151 is located ~7.3 Å from Fe1, a distance too far for direct proton transfer. Given that the pH dependencies of k_2 and k_3 were fit to models involving single or double protonation events, it is therefore unlikely that this residue is involved. T213 is of particular interest because this residue is conserved throughout the bacterial multicomponent monooxygenase family, can undergo redox-dependent conformational changes (41, 42), and is invoked to participate in proton transfer in cytochromes P450 (43–45). Although T213 appears to be a good candidate, it is unlikely to have such a low pK_a value in a hydrophobic active site, and thus proton transfer probably does not occur directly from this residue. Because none of these amino acids particularly stand out as potential proton donors, and because deprotonation of these residues would result in charge separation in a surrounding hydrophobic environment, it is unlikely that the source of protons in either step is an amino acid side chain.

The most likely alternative is an active site water molecule. Although the pK_a of water is 15.7, this value is significantly reduced to near neutral by coordination to iron (46, 47) and/or though strong hydrogen-bonding interactions with active site residues. Possible candidates for iron-bound proton donors with pK_a values in the range of those measured for k_2 and k_3 include terminal aqua or hydroxo groups and/or bridging hydroxide moieties. Terminal Fe(III)-aqua complexes tend to be acidic; for example, the pK_a for deprotonation of $[Fe(H_2O)_6]^{3+}$ is 2.74 and the species exists as $[Fe(OH)(H_2O)_5]^{2+}$ at neutral pH (48). However, such pK_a values are strongly influenced by the coordination environment of the iron(III) ion, aqua complex of which can exist at neutral pH. Indeed, crystallographic and spectroscopic studies support a terminal water molecule bound to Fe1 in the resting state of MMOH (49). Terminal Fe(III)-hydroxo units are less acidic than their aqua counterparts, but the pK_a values of these units also vary with ligand set and can readily form neutral pH. Interestingly, the hydroxide ligand of $[Fe(H_2O)_4(OH)_2]^+$ is deprotonated with pK_a ~6 due to formation of an oxo-bridged dinuclear species (47). These possibilities are particularly attractive because proton donation from iron-bound water to another ligand on the diiron center (vide infra) would maintain a charge-neutral core and not require the energetically unfavorable act of delivering a proton from solvent to the hydrophobic active site cavity.

Additionally, the proximity of such a proton donor to the acceptor would be in a range acceptable for direct transfer and no intermediates would be required.

Alternatively, proton transfer could occur from a water molecule that resides in the active site but is not directly coordinated to the diiron center. If such were the case, it is possible that the energetic cost of proton delivery within the hydrophobic active site could be compensated by the thermodynamically favorable interaction between MMOB and MMOH during the reductive phase of catalysis. Recent structural characterization of a hydroxylase-regulatory protein complex in the toluene 4-monooxygenase system demonstrated the residence of an ordered water molecule that is hydrogen-bonded to the conserved threonine residue T201 thought to be involved in proton translocation (vide supra) in the oxidized and reduced states of the enzyme only when the regulatory protein was bound (38). There are several other water molecules in close proximity to the active site that could also contribute protons during the P^* to H_{peroxo} and H_{peroxo} to Q processes (50).

Proton Acceptors

For possible proton acceptors, we favor a mechanism in which protons are transferred to an active site species, possibly accompanied by a slight conformational change. Again, to maintain charge neutrality in the hydrophobic active site cavity it is unlikely that protons would be transferred to amino acid side chains, except if these residues were coordinated to iron and the iron unit could maintain a charge neutral state. Possibilities include bound carboxylates, histidines, hydroxide, or oxide, as well as the O–O moiety prior to bond cleavage.

Of particular interest is the redox-dependent shifting carboxylate ligand E243. In reduced MMOH, residue coordinates in a bidentate fashion to Fe2 while bridging the two irons atoms, but binds in a monodentate fashion only to Fe2 when the hydroxylase is oxidized (41). This ligand most likely will depart from its bridging position during reaction of H_{red} with O_2 to open a coordination site for O_2 and to accommodate any other active site structural changes. Carboxylate shifts of this kind play an important role in controlling the reactivity of diiron proteins and synthetic model systems (41, 51, 52). For example, protonation of E243 might cause it to dissociate from its bridging position, decreasing steric bulk at the active site and enabling rearrangement of the oxygenated diiron site to accommodate Q. Although carboxylate residues are acidic, the thermodynamic driving force for conversion of H_{peroxo} to Q could drive the protonation reaction energetically. Additionally, the hydrophobic nature of the active site might raise the pK_a of E243 to near neutrality.

The other amino acid-based possibility is a coordinating histidine residue. Transfer of a proton to H147 or H246 could cause these ligands to dissociate, which in turn would modulate the redox behavior of the diiron core, providing a thermodynamic driving force for electronic changes of the O_2-diiron unit and possibly promoting O–O bond scission. Recent crystallographic studies on the diiron protein *Hedera helix* 18:0 Δ^9-desaturase demonstrated that a histidine ligand undergoes redox-dependent decoordination of exactly this kind (53). The pK_a values of histidine residues are within range of those measured for k_2 and k_3. It is also possible that protons are transferred to terminal or bridging iron-bound aqua-, hydroxo-, or oxo- species (vide supra). Transfer of a proton to a terminal hydroxo group by this type of mechanism yields a $[Fe^{IV}_2(\mu\text{-}O)_2]^{4+}$, Q-like, species in a synthetic model system (54).

Protons could also be transferred directly to the O–O moiety in these steps. This type of mechanism would result in a hydroperoxo intermediate and facilitate heterolytic O–O bond cleavage as shown in Scheme 1b. A similar mechanism is invoked in cytochromes P450 (27). However, the result of recent theoretical studies on the peroxodiiron species in RNR

and a mutant form of RNR suggest that H^+ addition to the O–O unit does not result in a stable hydroperoxo species and instead causes O–O bond scission in this enzyme (55).

Identity of P*

Reactions of $MMOH_{red}$:2B + O_2 performed in the presence of high (≥760 μM) concentrations of methane have provided for the first time in the *Mc* enzyme system direct kinetic evidence for the presence of two species that precede Q formation, P* and H_{peroxo}. Comparison of the data reported here to previous Mössbauer and optical spectroscopic studies are revealing. Mössbauer spectroscopy identified a single peroxodiiron(III) intermediate with $k_{form} \approx 25\ s^{-1}$, $k_{decay} = 0.45\ s^{-1}$, and $t_{max} = 156$ ms at 4 °C (7). Optical spectroscopic experiments also provided evidence for a single peroxodiiron(III) species, but this species was characterized by quite different kinetic parameters $k_{form} \approx 1.6\ s^{-1}$, $k_{decay} = 0.40\ s^{-1}$ and $t_{max} = 1$–2 s at 4 °C (10). To reconcile the dramatic difference in formation rate constants observed by these two methods, we proposed the presence of two peroxodiiron(III) species characterized by similar Mössbauer parameters, the first of which was not observable by optical spectroscopy (10). Through analysis of data collected in the presence of high concentrations of methane, we were able to reveal the spectrum of P* and provide the first optical evidence for this H_{peroxo} precursor. Speciation plots derived from our data lead to the prediction that the first of these species, P*, has $t_{max} = 370$ ms while the second, H_{peroxo}, is characterized by $t_{max} = 2.1$ s, which is reasonably consistent with the results obtained previously (Fig. S12). On the other hand, speciation plots derived from model (ii) are not consistent with these data, bolstering the argument that this model is not correct (Fig. S13).

Although this work helps reconcile the differences observed between the two forms of spectroscopy, the rate of P* formation measured here is still much slower than that obtained by analysis of the Mössbauer signal. Due to limitations of our instrumentation, the value of k_1' measured here is almost certainly underestimated (and the t_{max} of P* overestimated) by the fact P* has accumulated considerably in the dead time, as evidenced by the fact that the starting absorbances at 420 nm and 720 nm are much greater than those expected for H_{red} (Fig. 2). Therefore, P* might evolve directly from H_{red}, but these data do not rule out the possibility that there is an additional undetected intermediate that forms prior to P*. Similar reasoning led to the proposal of intermediate O in *Mt* MMOH (4, 56).

Because Mössbauer spectroscopy only identified one intermediate, it is possible that P* and H_{peroxo} exhibit indistinguishable Mössbauer parameters. However, Mössbauer data were not reported in the 0.5–3 s time regime in which H_{peroxo} maximally accumulates. Without further analysis we cannot rule out the possibility of distinct parameters for this intermediate. One certainty based on data collected before 0.5 s and the similar t_{max} values of the species characterized by Mössbauer spectroscopy and P* is that this intermediate is characterized by $\delta = 0.66$ mm/s and $\Delta E_Q = 1.51$ mm/s. Similar Mössbauer parameters have been assigned to a synthetic, structurally characterized model (μ-1,2-peroxo)diiron(III) model complex supported by a tris(pyrazolyl)borate ligand scaffold (57) as well as the peroxodiiron(III) intermediate generated in the W48A/D84E variant of RNR-R2 that are assigned μ-peroxide binding geometries (12, 58). The absorbance of P* around 720 nm ($\varepsilon = 1250\ M^{-1}\ cm^{-1}$) is similar to those of well-characterized peroxodiiron(III) species in enzymes (10, 15, 42, 59, 60) and model systems (57, 61) assigned as peroxo-to-Fe(III) charge transfer transitions. Because of its spectroscopic similarities to those of known enzyme intermediates and model complexes, P* is likely to contain a peroxodiiron(III) unit. Another possibility is a mixed-valent Fe(II)Fe(III) superoxide complex, but this assignment is less likely because its Mössbauer spectrum should exhibit two distinct quadrupole doublets because the unpaired electrons in this system are expected to be valence localized.

The presence of two detectable intermediates that precede Q formation in MMOH from *Mt* was previously reported (4). The first of these species, P^*, forms directly from O decay at a rate identical to that of H_{red} decay measured by EPR spectroscopy (29) and proceeds to intermediate P. The second, P, was assumed to absorb minimally at 430 nm, the wavelength at which the data were collected, based on two observations. Firstly, a phase corresponding to P^* to P conversion was not necessary to fit data monitored in the absence of substrate, which were modeled well by three phases attributed to O to P^*, P to Q, and Q to H_{ox} conversion. Secondly, the formation of P contributed only a very small amount to the total amplitude of the absorbance rise phase when experiments were performed in the presence of high concentrations of furan to remove contributions from Q. The authors argued that the absorbance attributed to this intermediate (H_{peroxo}) at 420 nm in previous reports from our group on the *Mc* system was an artifact from absorption of Q at this wavelength. However, the data presented here, collected in the presence of methane in which there is no possibility of interference from Q, now provide definitive evidence that H_{peroxo} does indeed absorb strongly at this wavelength and disagree with the results from the *Mt* enzyme.

Nature of P^* to H_{peroxo} Conversion

The similarities of the P^* optical extinction coefficients to those of H_{peroxo} suggests that these intermediates are electronically and geometrically similar. Analysis of the pH dependent data indicates that a single proton is transferred during the rate-limiting step of P^* to H_{peroxo} conversion and that this protonation event, with a pK_a of 7.2, must occur for H_{peroxo} to form. The conversion may involve direct protonation of the O–O moiety or a small conformational change that is ultimately necessary for Q formation (vide supra). Formation of a hydroperoxo by protonation of the peroxide, however, would most likely alter the energy of the peroxo-to-iron(III) charge transfer band of P^* and probably the Mössbauer parameters. It is therefore is more reasonable that P^* to H_{peroxo} occurs by protonation of an active site residue in a manner that does not require thermodynamically unfavorable solvation of separated charges. Recent theoretical studies on the peroxo intermediates of RNR and its W48A/Y122F variant (62) find that proton transfer from an iron-bound water molecule to a carboxylate ligand, or solvent-derived proton addition to a carboxylate ligand, are energetically feasible and both would result in the stable peroxodiiron(III) species (55). In the former option, proton transfer occurs with concomitant opening of the bidentate carboxylate bridge. In the latter, stable structures were obtained only when the carboxylate was bridging the iron atoms, and the protonation event did not affect the optical spectrum or the Mössbauer isomer shifts to a significant degree. One possible mechanism of P^* to H_{peroxo} conversion based on these findings, as well as the kinetic and pH dependence data reported here, is illustrated in Scheme 6.

Nature of H_{peroxo} to Q Conversion

The ability of sMMO to provide a single oxygen atom from molecular oxygen for incorporation into hydrocarbon substrates depends on its ability to cleave the O–O bond and form a potent oxidant. O–O bond scission occurs concomitant with H_{peroxo} to Q conversion; however, the mechanistic details of this step are not well understood. Scheme 1 depicts two simplified mechanisms for this event in which O–O bond cleavage processes are either homolytic (1a) or heterolytic (1b). In principle, the products of steady state reaction of the enzyme with substrate using $^{18}O_2$ might discriminate between these mechanisms. The product is expected to be completely labeled if both oxygen atoms of Q derive from O_2, but might contain a mixture of ^{16}O and ^{18}O labels if a solvent-derived oxygen atom were incorporated into Q. Such a study did reveal that 100% of label is incorporated into methanol (63), in support of a homolytic mechanism. However, this interpretation is not definitive, because stereoelectronic factors might enforce reactivity with the oxygen atom

directed toward the active site cavity, which might retain 100% of the label for incorporation into product, even when the O–O bond is cleaved heterolytically.

Analysis of the pH dependence data suggests that two protons can be transferred during the rate-limiting step of H_{peroxo} to Q conversion. Whereas one protonation event, with a pK_a of 7.9, is crucial for Q formation, the second, with a pK_a of 7.0, accelerates the rate but is not required. The absolute necessity of the first protonation step suggests that it takes place directly at the iron center and facilitates O–O bond cleavage. One possible mechanism of H_{peroxo} to Q conversion is depicted in Scheme 7. In this mechanism, a first and necessary proton transfer occurs from a terminal hydroxide to result in formation of a hydroperoxide and a bridging oxide. The O–O bond of the hydroperoxide can then be cleaved homolytically to form a transient Fe_2^{IV} species with a terminal hydroxide. Proton transfer from E243 could then generate Q. However, because this step occurs after presumably irreversible O–O bond cleavage, it is not expected to be detected in our measurements. Whereas this single proton transfer pathway is sufficient for Q formation, double protonation of the peroxide moiety might lead to more rapid O–O bond scission. This event is characterized by the second protonation step with pK_a of 7.0. The pK_a values measured in this work support this hypothesis (vide supra). Although the O–O bond cleavage steps are depicted to occur in a homolytic manner, it is possible that this event could also take place heterolytically, in which a transient $Fe^{V}Fe^{III}$ terminal oxo species is formed (64).

Mechanism of Q Decay

The mechanism of Q decay in the absence of substrates has remained an enigma for many years. This reaction requires the acquisition of two protons and two electrons by the diiron active site, but the source of these substrates is unknown. Protons could derive from solvent. Because there are no exogenous electron donors in the reaction mixture, the electrons must come from the protein itself. Two possible protein-based reductants can be envisioned in this system, amino acid side chains and/or the diiron(II) center in the neighboring protomer (Scheme 8). For the former, Q could abstract electrons and possibly protons from nearby amino acid residue(s). This process could be achieved either by direct oxidative hydroxylation of a proximal amino acid residue (Scheme 8a) or by two stepwise electron transfer events, most likely proton-coupled (Scheme 8b). The latter option would generate a proton-based radical and a mixed valent $Fe^{III}Fe^{IV}$ center and is reminiscent of chemistry occurring in the R2 subunit of RNR, in which the nearby amino acids W48 and Y122 can donate electrons to the iron site during formation of the $Fe^{III}Fe^{IV}$ intermediate X (Scheme 8c) (65, 66). For the second option, it is possible that electrons from a neighboring diiron(II) center could quench Q, as proposed to explain the formation of mixed valent $Fe^{III}Fe^{IV}$ and $Fe^{II}Fe^{III}$ species in the reaction of a synthetic tetracarboxylate diiron(II) model system with O_2 (67). If a diiron(II) center is present in the active site of one hydroxylase protomer when Q has formed in the other, intramolecular electron transfer between the diiron centers could lead to formation of two diiron(III) species. Indeed, a large population of H_{red} decays to H_{ox} by an unknown mechanism on a timescale that is much slower than the O_2 activation phase (7) and therefore a significant portion diiron(II) is available to donate electrons to Q. This possibility seems less likely considering that the distance between the two iron centers is ~ 45 Å (49), an unprecedented distance for protein electron transfer.

The data reported here suggest for the first time an intermediate species, Q*, which forms as a result of Q decay in the absence of hydrocarbon substrates. Two lines of evidence indicate that Q* is an intermediate on the Q decay pathway rather than a functionally significant species. First, Q* is not capable of methane oxidation and second, Q reacts with methane and does so by a mechanism that does proceed through Q*. Based on the mechanistic possibilities discussed above, this intermediate could be a $Fe^{III}Fe^{IV}$ unit and a protein-based radical or a combination of $Fe^{III}Fe^{IV}$ and $Fe^{II}Fe^{III}$ species, both of which are consistent with

the optical spectrum of Q^*. Other alternatives include a distinct diiron(IV) species that is more thermodynamically stable than Q, or an oxo-bridged diiron(III) species. The latter can be ruled out because the optical spectrum of Q^* is not typical of these types of units and because the decay of Q^* does not involve rate-limiting proton transfer, which would be expected for conversion of an oxo-bridged core to hydroxo-bridged H_{ox}. Additionally, Q is not expected to decay by hydroxylation, for this type of mechanism is likely to occur in a concerted manner with no stable intermediates characterized by distinct optical spectra, as noted for the oxidation of methane and adventitious substrates (4, 9–11, 68). Spectroscopic characterization of intermediate Q^* is currently in progress to investigate the nature of this species.

The present results represent the first evidence of Q^*. Kinetic studies performed previously in MOPS buffer reported a Q decay rate of 0.05 s^{-1} (7, 10), which is considerably faster than that measured here (0.01 s^{-1}). The fact that Q decay is faster in these earlier studies suggests oxidization by this intermediate of a reaction mixture component no present in the current experiments. Such a component should lead to a mechanism of Q decay that does not proceed through Q^*, as occurs for methane (vide supra). Because phosphate buffer was used in the present work, it is possible that Q oxidized MOPS in the earlier studies. Double-mixing stopped-flow experiments reveal, however, that although Q does react with MOPS, this process is very slow and cannot account for the significant differences in behavior at the concentrations employed. Additionally, single-mixing stopped-flow studies performed in MOPS in the present work continue to provide evidence of Q^*. It is possible that older preparations in MOPS contained a hydrocarbon impurity that reacted with Q, but the reason for its decay of Q in previous studies remains unknown.

CONCLUDING REMARKS

The data presented here provide conclusive kinetic evidence for the presence of multiple oxygenated diiron intermediates that accumulate during the catalytic cycle of MMOH and demonstrate that P^* to H_{peroxo} and H_{peroxo} to Q conversions are both pH dependent. These studies and recent investigations of other BMMs and model complexes highlight the complexity of the systems, particularly with respect to the time-dependent coordination and activation of O_2, proton translocation and electron transfer, and hydrocarbon entry and egress. Taken together, the present study and prior work on the *Mt* system have now begun to converge, providing a framework for understanding MMOH catalysis and a paradigm for interpreting kinetic data in this system. However, questions raised by these studies indicate the need for further kinetic and spectroscopic evaluation. For example, the nature of the proton transfer events during P^* to H_{peroxo} and H_{peroxo} to Q conversion and the electronic and geometric identities of the four intermediates are pressing, unsolved questions. Efforts are therefore under way to reinvestigate the spectroscopic properties and protonation states of P^*, H_{peroxo}, and Q and to determine those of Q^*.

Supplementary Material

Refer to Web version on PubMed Central for supplementary material.

Acknowledgments

This work was funded by grant GM032134 from the National Institute of General Medical Sciences to S. J. L. C.E.T. was supported under a N. I. H. Interdepartmental Biotechnology Training Grant T32 GM08334. The authors thank Dr. R. K. Behan and Ms. W. J. Song for helpful discussions.

REFERENCES

1. Merkx M, Kopp DA, Sazinsky MH, Blazyk JL, Müller J, Lippard SJ. Dioxygen Activation and Methane Hydroxylation by Soluble Methane Monooxygenase: A Tale of Two Irons and Three Proteins. Angew. Chem. Int. Ed. 2001; 40:2782–2807.
2. Hakemian AS, Rosenzweig AC. The Biochemistry of Methane Oxidation. Annu. Rev. Biochem. 2007; 76:223–241. [PubMed: 17328677]
3. Murrell JC, Gilbert B, McDonald IR. Molecular Biology and Regulation of Methane Monooxygenase. Arch. Microbiol. 2000; 173:325–332. [PubMed: 10896210]
4. Brazeau BJ, Lipscomb JD. Kinetics and Activation Thermodynamics of Methane Monooxygenase Compound Q Formation and Reaction with Substrates. Biochemistry. 2000; 39:13503–13515. [PubMed: 11063587]
5. Lee S-K, Fox BG, Froland WA, Lipscomb JD, Münck E. A Transient Intermediate of the Methane Monooxygenase Catalytic Cycle Containing an $Fe^{IV}Fe^{IV}$ Cluster. J. Am. Chem. Soc. 1993; 115:6450–6451.
6. Lee S-K, Nesheim JC, Lipscomb JD. Transient Intermediates of the Methane Monooxygenase Catalytic Cycle. J. Biol. Chem. 1993; 268:21569–21577. [PubMed: 8408008]
7. Liu KE, Valentine AM, Wang D, Huynh BH, Edmondson DE, Salifoglou A, Lippard SJ. Kinetic and Spectroscopic Characterization of Intermediates and Component Interactions in Reactions of Methane Monooxygenase from *Methylococcus capsulatus* (Bath). J. Am. Chem. Soc. 1995; 117:10174–10185.
8. Liu KE, Wang D, Huynh BH, Edmondson DE, Salifoglou A, Lippard SJ. Spectroscopic Detection of Intermediates in the Reaction of Dioxygen with Reduced Methane Monooxygenase Hydroxylase from *Methylococcus capsulatus* (Bath). J. Am. Chem. Soc. 1994; 116:7465–7466.
9. Beauvais LG, Lippard SJ. Reactions of the Peroxo Intermediate of Soluble Methane Monooxygenase Hydroxylase with Ethers. J. Am. Chem. Soc. 2005; 127:7370–7378. [PubMed: 15898785]
10. Valentine AM, Stahl SS, Lippard SJ. Mechanistic Studies of the Reaction of Reduced Methane Monooxygenase Hydroxylase with Dioxygen and Substrates. J. Amer. Chem. Soc. 1999; 121:3876–3887.
11. Ambundo EA, Friesner RA, Lippard SJ. Reactions of Methane Monooxygenase Intermediate Q with Derivatized Methanes. J. Am. Chem. Soc. 2002; 124:8770–8771. [PubMed: 12137510]
12. Moënne-Loccoz P, Baldwin J, Ley BA, Loehr TM, Bollinger JM Jr. O_2 Activation by Non-Heme Diiron Proteins: Identification of a Symmetric μ-1,2-Peroxide in a Mutant of Ribonucleotide Reductase. Biochemistry. 1998; 37:14659–14663. [PubMed: 9778340]
13. Skulan AJ, Brunold TC, Baldwin J, Saleh L, Bollinger JM Jr. Solomon EI. Nature of the Peroxo Intermediate of the W48F/D84E Ribonucleotide Reductase Variant: Implications for O_2 Activation by Binuclear Non-Heme Iron Enzymes. J. Am. Chem. Soc. 2004; 126:8842–8855. [PubMed: 15250738]
14. Moënne-Loccoz P, Krebs C, Herlihy K, Edmondson DE, Theil EC, Huynh BH, Loehr TM. The Ferroxidase Reaction of Ferritin Reveals a Diferric μ-1,2 Bridging Peroxide Intermediate in Common with Other O_2-Activating Non-Heme Diiron Proteins. Biochemistry. 1999; 38:5290–5295. [PubMed: 10220314]
15. Broadwater JA, Ai J, Loehr TM, Sanders-Loehr J, Fox BG. Peroxodiferric Intermediate of Stearoyl-Acyl Carrier Protein Δ^9 Desaturase: Oxidase Reactivity during Single Turnover and Implications for the Mechanism of Desaturation. Biochemistry. 1998; 37:14664–14671. [PubMed: 9778341]
16. Vu VV, Emerson JP, Martinho M, Kim YS, Münck E, Park MH, Que L Jr. Human Deoxyhypusine Hydroxylase, an Enzyme Involved in Regulating Cell Growth, Activates O_2 with a Nonheme Diiron Center. Proc. Natl. Acad. Sci. USA. 2009; 106:14814–14819. [PubMed: 19706422]
17. Han W-G, Noodleman L. Structural Model Studies for the Peroxo Intermediate P and the Reaction Pathway from P → Q of Methane Monooxygenase Using Broken-Symmetry Density Functional Calculations. Inorg. Chem. 2008; 47:2975–2986. [PubMed: 18366153]

18. Gherman BF, Baik M-H, Lippard SJ, Friesner RA. Dioxygen Activation in Methane Monooxygenase: A Theoretical Study. J. Am. Chem. Soc. 2004; 126:2978–2990. [PubMed: 14995216]
19. Rinaldo D, Philipp DM, Lippard SJ, Friesner RA. Intermediates in Dioxygen Activation by Methane Monooxygenase: A QM/MM Study. J. Am. Chem. Soc. 2007; 129:3135–3147. [PubMed: 17326634]
20. Siegbahn PEM. O–O Bond Cleavage and Alkane Hydroxylation in Methane Monooxygenase. J. Biol. Inorg. Chem. 2001; 6:27–45. [PubMed: 11191221]
21. Shu L, Nesheim JC, Kauffmann K, Münck E, Lipscomb JD, Que L Jr. An $Fe_2^{IV}O_2$ Diamond Core Structure for the Key Intermediate Q of Methane Monooxygenase. Science. 1997; 275:515–518. [PubMed: 8999792]
22. Baik M-H, Newcomb M, Friesner RA, Lippard SJ. Mechanistic Studies on the Hydroxylation of Methane by Methane Monooxygenase. Chem. Rev. 2003; 103:2385–2419. [PubMed: 12797835]
23. Gherman BF, Lippard SJ, Friesner RA. Substrate Hydroxylation in Methane Monooxygenase: Quantitative Modeling via Mixed Quantum Mechanics/Molecular Mechanics Techniques. J. Am. Chem. Soc. 2005; 127:1025–1037. [PubMed: 15656641]
24. Baik M-H, Gherman BF, Friesner RA, Lippard SJ. Hydroxylation of Methane by Non-Heme Diiron Enzymes: Molecular Orbital Analysis of C-H Bond Activation by Reactive Intermediate Q. J. Am. Chem. Soc. 2002; 124:14608–14615. [PubMed: 12465971]
25. Halfen JA, Mahapatra S, Wilkinson EC, Kaderli S, Young VG Jr. Que L Jr. Zuberbühler AD, Tolman WB. Reversible Cleavage and Formation of the Dioxygen O–O Bond Within a Dicopper Complex. Science. 1996; 271:1397–1400. [PubMed: 8596910]
26. Lewis EA, Tolman WB. Reactivity of Dioxygen-Copper Systems. Chem. Rev. 2004; 104:1047–1076. [PubMed: 14871149]
27. Denisov IG, Makris TM, Sligar SG, Schlichting I. Structure and Chemistry of Cytochrome P450. Chem. Rev. 2005; 105:2253–2277. [PubMed: 15941214]
28. Nam W. High-Valent Iron(IV)-Oxo Complexes of Heme and Non-Heme Ligands in Oxygenation Reactions. Acc. Chem. Res. 2007; 40:522–531. [PubMed: 17469792]
29. Lee S-K, Lipscomb JD. Oxygen Activation Catalyzed by Methane Monooxygenase Hydroxylase Component: Proton Delivery during the O–O Bond Cleavage Steps. Biochemistry. 1999; 38:4423–4432. [PubMed: 10194363]
30. Coufal DE, Blazyk JL, Whittington DA, Wu WW, Rosenzweig AC, Lippard SJ. Sequencing and Analysis of the *Methylococcus capsulatus* (Bath) Soluble Methane Monooxygenase Genes. Eur. J. Biochem. 2000; 267:2174–2185. [PubMed: 10759840]
31. Kopp DA, Gassner GT, Blazyk JL, Lippard SJ. Electron-Transfer Reactions of the Reductase Component of Soluble Methane Monooxygenase from *Methylococcus capsulatus* (Bath). Biochemistry. 2001; 40:14932–14941. [PubMed: 11732913]
32. Wilhelm E, Battino R, Wilcock RJ. Low-Pressure Solubility of Gases in Liquid Water. Chem. Rev. 1977; 77:219–262.
33. Beechem JM. Global Analysis of Biochemical and Biophysical Data. Methods Enzymol. 1992; 210:37–54. [PubMed: 1584042]
34. Murray LJ, Lippard SJ. Substrate Trafficking and Dioxygen Activation in Bacterial Multicomponent Monooxygenases. Acc. Chem. Res. 2007; 40:466–474. [PubMed: 17518435]
35. Fersht, A. Enzyme Structure and Mechanism. 2nd ed.. W. H. Freeman and Co.; New York, NY: 1977. Chapter 5.
36. Quinn, DM.; Sutton, LD. Theoretical Basis and Mechanistic Utility of Solvent Isotope Effects. In: Cook, PF., editor. Enzyme Mechanism from Isotope Effects. CRC Press; Boca Raton: 1991.
37. Tinberg, C.; Lippard, SJ. 2009. Unpublished Results
38. Bailey LJ, McCoy JG, Phillips GN Jr. Fox BG. Structural Consequences of Effector Protein Complex Formation in a Diiron Hydroxylase. Proc. Natl. Acad. Sci. USA. 2008; 105:19194–19198. [PubMed: 19033467]
39. Schowen KB, Schowen RL. Solvent Isotope Effects on Enzyme Systems. Methods Enzymol. 1982; 87:551–606. [PubMed: 6294457]

40. Dunietz BD, Beachy MD, Cao Y, Whittington DA, Lippard SJ, Friesner RA. Large Scale ab Initio Quantum Chemical Calculation of the Intermediates in the Soluble Methane Monooxygenase Catalytic Cycle. J. Am. Chem. Soc. 2000; 122:2828–2839.
41. Sazinsky MH, Lippard SJ. Correlating Structure with Function in Bacterial Multicomponent Monooxygenases and Related Diiron Proteins. Acc. Chem. Res. 2006; 39:558–566. [PubMed: 16906752]
42. Song WJ, Behan RK, Naik SG, Huynh BH, Lippard SJ. Characterization of a Peroxodiiron(III) Intermediate in the T201S Variant of Toluene/*o*-Xylene Monooxygenase Hydroxylase from *Pseudomonas sp*. OX1. J. Am. Chem. Soc. 2009; 131:6074–6075. [PubMed: 19354250]
43. Altarsha M, Benighaus T, Kumar D, Thiel W. How is the Reactivity of Cytochrome P450cam Affected by Thr252X Mutation? A QM/MM Study for X = Serine, Valine, Alanine, Glycine. J. Am. Chem. Soc. 2009; 131:4755–4763. [PubMed: 19281168]
44. Imai M, Shimada H, Watanabe Y, Matsushima-Hibiya Y, Makino R, Koga H, Horiuchi T, Ishimura Y. Uncoupling of the Cytochrome P-450cam Monooxygenase Reaction by a Single Mutation, Threonine-252 to Alanine or Valine: A Possible Role of the Hydroxy Amino Acid in Oxygen Activation. Proc. Natl. Acad. Sci. USA. 1989; 86:7823–7827. [PubMed: 2510153]
45. Raag R, Martinis SA, Sligar SG, Poulos TL. Crystal Structure of the Cytochrome P-450$_{CAM}$ Active Site Mutant Thr252Ala. Biochemistry. 1991; 30:11420–11429. [PubMed: 1742281]
46. Holm RH, Kennepohl P, Solomon EI. Structural and Functional Aspects of Metal Sites in Biology. Chem. Rev. 1996; 96:2239–2314. [PubMed: 11848828]
47. Lippard, SJ.; Berg, JM. Priciples of Bioinorganic Chemistry. University Science Books; Mill Valley, CA: 1994. p. 24-26.
48. Cotton, FA.; Wilkinson, G.; Murillo, CA.; Bochmann, M. Advanced Inorganic Chemistry. 6th ed.. John Wiley & Sons, Inc; New York: 2003. p. 787
49. Rosenzweig AC, Frederick CA, Lippard SJ, Nordlund P. Crystal Structure of a Bacterial Non-Haem Iron Hydroxylase that Catalyses the Biological Oxidation of Methane. Nature. 1993; 366:437–543.
50. Whittington DA, Lippard SJ. Crystal Structures of the Soluble Methane Monooxygenase Hydroxylase from *Methylococcus capsulatus* (Bath) Demonstrating Geometrical Variability at the Dinuclear Iron Active Site. J. Am. Chem. Soc. 2001; 123:827–838. [PubMed: 11456616]
51. Rardin RL, Tolman WB, Lippard SJ. Monodentate Carboxylate Complexes and the Carboxylate Shift - Implications for Polymetalloprotein Structure and Function. New J. Chem. 1991; 15:417–430.
52. Tshuva EY, Lippard SJ. Synthetic Models for Non-Heme Carboxylate-Bridged Diiron Metalloproteins: Strategies and Tactics. Chem. Rev. 2004; 104:987–1012. [PubMed: 14871147]
53. Shanklin J, Guy JE, Mishra G, Lindqvist Y. Desaturases: Emerging Models for Understanding Functional Diversification of Diiron-Containing Enzymes. J. Biol. Chem. 2009; 284:18559–18563. [PubMed: 19363032]
54. Xue G, Fiedler AT, Martinho M, Münck E, Que L Jr. Insights into the P-to-Q Conversion in the Catalytic Cycle of Methane Monooxygenase from a Synthetic Model System. Proc. Natl. Acad. Sci. USA. 2008; 105:20615–20620.
55. Jensen KP, Bell CBI, Clay MD, Solomon EI. Peroxo-Type Intermediates in Class 1 Ribonucleotide Reductase and Related Binuclear Non-Heme Iron Enzymes. J. Am. Chem. Soc. 2009; 131:12155–12171. [PubMed: 19663382]
56. Liu Y, Nesheim JC, Lee S-K, Lipscomb JD. Gating Effects of Component B on Oxygen Activation by the Methane Monooxygenase Hydroxylase Component. J. Biol. Chem. 1995; 270:24662–24665. [PubMed: 7559577]
57. Kim K, Lippard SJ. Structure and Mössbauer Spectrum of a (μ-1,2-Peroxo)bis(μ-carboxylato)diiron(III) Model for the Peroxo Intermediate in the Methane Monooxygenase Hydroxylase Reaction Cycle. J. Am. Chem. Soc. 1996; 118:4914–4915.
58. Baldwin J, Krebs C, Saleh L, Stelling M, Huynh BH, Bollinger JM Jr. Riggs-Gelasco P. Structural Characterization of the Peroxodiiron(III) Intermediate Generated during Oxygen Activation by the W48A/D84E Variant of Ribonucleotide Reductase Protein R2 from *Escherichia coli*. Biochemistry. 2003; 42:13269–13279. [PubMed: 14609338]

59. Bollinger JM Jr. Krebs C, Vicol A, Chen S, Ley BA, Edmondson DE, Huynh BH. Engineering the Diiron Site of *Escherichia coli* Ribonucleotide Reductase Protein R2 to Accumulate an Intermediate Similar to H_{peroxo}, the Putative Peroxodiiron(III) Complex from the Methane Monooxygenase Catalytic Cycle. J. Am. Chem. Soc. 1998; 120:1094–1095.
60. Pereira AS, Small W, Krebs C, Tavares P, Edmondson DE, Theil EC, Huynh BH. Direct Spectroscopic and Kinetic Evidence for the Involvement of a Peroxodiferric Intermediate during the Ferroxidase Reaction in Fast Ferritin Mineralization. Biochemistry. 1998; 37:9871–9876. [PubMed: 9665690]
61. Yamashita M, Furutachi H, Tosha T, Fujinami S, Saito W, Maeda Y, Takahashi K, Tanaka K, Kitagawa T, Suzuki M. Regioselective Arene Hydroxylation Mediated by a (μ-Peroxo)diiron(III) Complex: A Functional Model for Toluene Monooxygenase. J. Am. Chem. Soc. 2007; 129:2. [PubMed: 17199259]
62. Saleh L, Krebs C, Ley BA, Naik S, Huynh BH, Bollinger JM Jr. Use of a Chemical Trigger for Electron Transfer to Characterize a Precursor to Cluster X in Assembly of the Iron-Radical Cofactor of *Escherichia coli* Ribonucleotide Reductase. Biochemistry. 2004; 43:5953–5964. [PubMed: 15147179]
63. Nesheim JC, Lipscomb JD. Large Kinetic Isotope Effects in Methane Oxidation Catalyzed by Methane Monooxygenase: Evidence for C-H Bond Cleavage in a Reaction Cycle Intermediate. Biochemistry. 1996; 35:10240–10247. [PubMed: 8756490]
64. Rowe GT, Rybak-Akimova EV, Caradonna JP. Unraveling the Reactive Species of a Functional Non-Heme Iron Monooxygenase Model Using Stopped-Flow UV-Vis Spectroscopy. Inorg. Chem. 2007; 46:10594–10606. [PubMed: 17988120]
65. Krebs C, Chen S, Baldwin J, Ley BA, Patel U, Edmondson DE, Huynh BH, Bollinger JM Jr. Mechanism of Rapid Electron Transfer during Oxygen Activation in the R2 Subunit of *Escherichia coli* Ribonucleotide Reductase. 2. Evidence for and Consequences of Blocked Electron Transfer in the W48F Variant. J. Am. Chem. Soc. 2000; 122:12207–12219.
66. Stubbe J, Nocera DG, Yee CS, Chang MCY. Radical Initiation in the Class 1 Ribonucleotide Reductase: Long-Range Proton-Coupled Electron Transfer? Chem. Rev. 2003; 103:2167–2201. [PubMed: 12797828]
67. Lee D, Du Bois J, Petasis D, Hendrich MP, Krebs C, Huynh BH, Lippard SJ. Formation of Fe(III)Fe(IV) Species from the Reaction between a Diiron(II) Complex and Dioxygen: Relevance to Ribonucleotide Reductase Intermediate X. J. Am. Chem. Soc. 1999; 121:9893–9894.
68. Tinberg, CE.; Lippard, SJ. Oxidation Reactions of Soluble Methane Monooxygenase Intermediates H_{peroxo} and Q Proceed by Distinct Mechanisms. 2009. Manuscript in Preparation

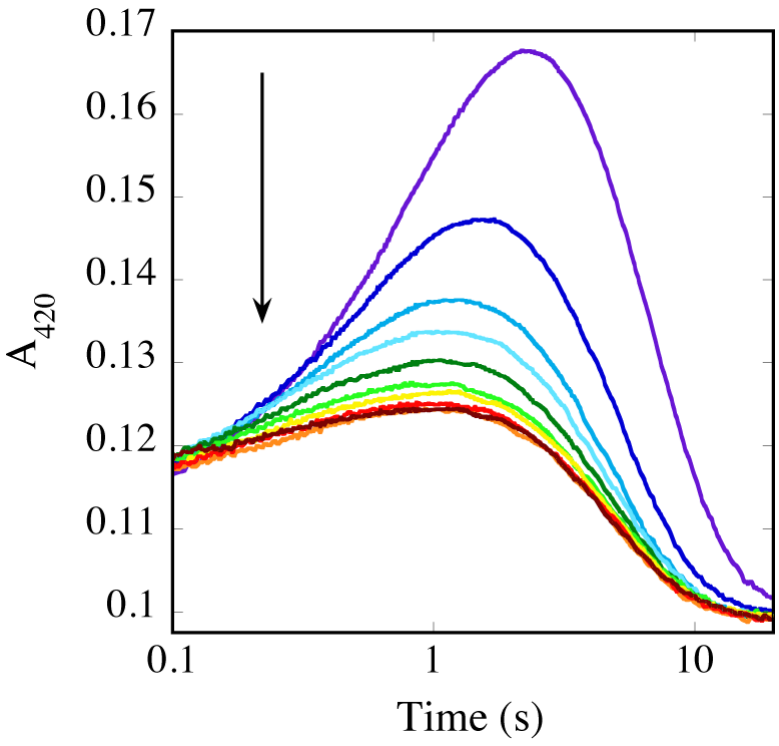

Figure 1.

Representative absorbance profiles for the reaction of 50 μM $MMOH_{red}$ with a mixture of O_2 and CH_4 in the presence of 2 equiv of MMOB at 4 °C and 420 nm. [CH_4] = 77 μM (purple), 154 μM (blue), 231 μM (cyan), 308 μM (aqua), 385 μM (dark green), 462 μM (light green), 500 μM (yellow), 539 μM (orange), 578 μM (red), 616 μM (maroon). Data collected on separate occasions with different batches of protein yielded similar results.

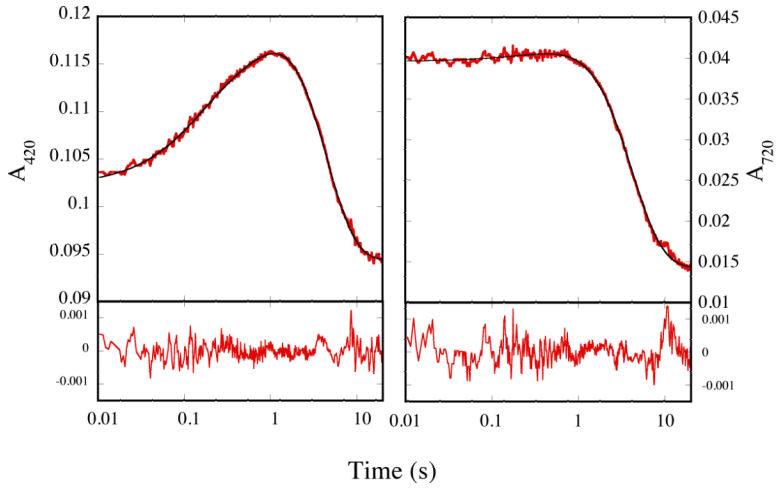

Figure 2.

Representative fits of data monitoring the reaction of $MMOH_{red}$ with O_2 in the presence of 578 mM CH_4 and 2 equiv MMOB at 4 °C. Data collected at 420 nm (left, red lines) and 720 nm (right, red lines) were fit simultaneously to the $H_{red} \rightarrow P^* \rightarrow H_{peroxo} \rightarrow H_{ox}$ model (eq 1). This method returned good fits (black lines) with acceptable residuals (bottom plots) and $\chi^2_{red} < 1.07 \times 10^{-7}$.

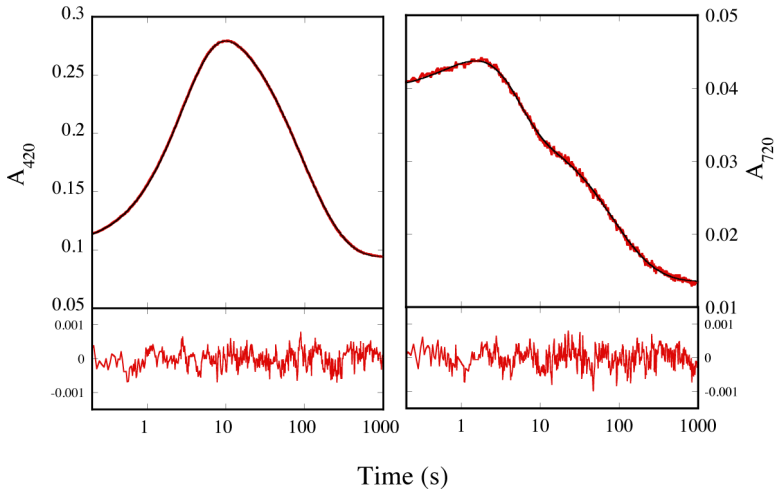

Figure 3.

Representative fits of data monitoring the reaction of $MMOH_{red}$ with O_2 in the presence of two equiv MMOB at 4 °C. Data collected at 420 nm (left, red lines) and 720 nm (right, red lines) were fit simultaneously to the $P^* \rightarrow H_{peroxo} \rightarrow Q \rightarrow Q^* \rightarrow H_{ox}$ model (eq 3). This method yielded good fits (black lines) with acceptable residuals (bottom plots) and $\chi^2_{red} < 8.14 \times 10^{-8}$.

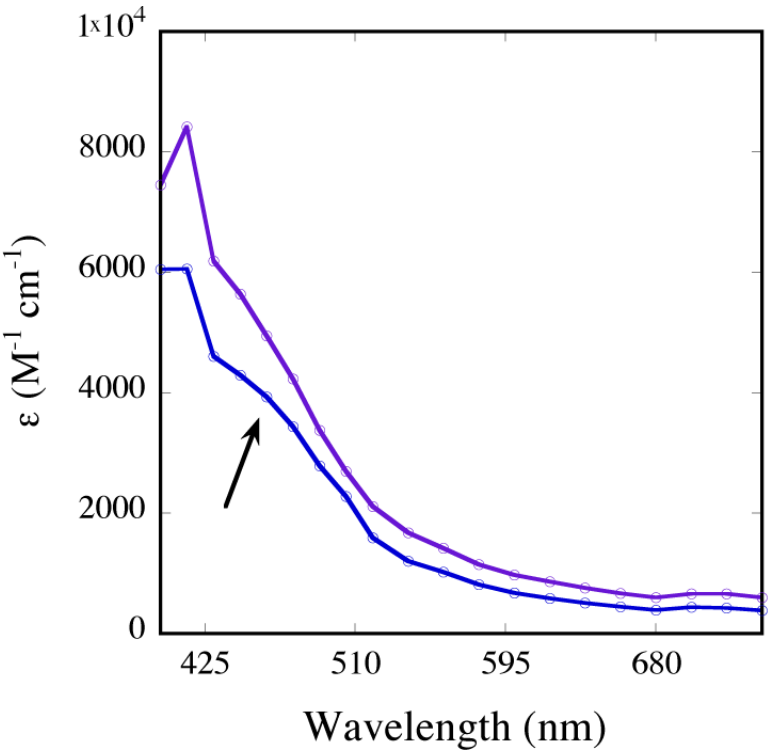

Figure 4.
Optical spectra of Q (purple) and Q* (blue). Spectra were obtained at 4 °C from data collected every 15 or 20 nm and analyzed by global fitting procedures described in the text. The arrow points to the 455 nm shoulder of Q*.

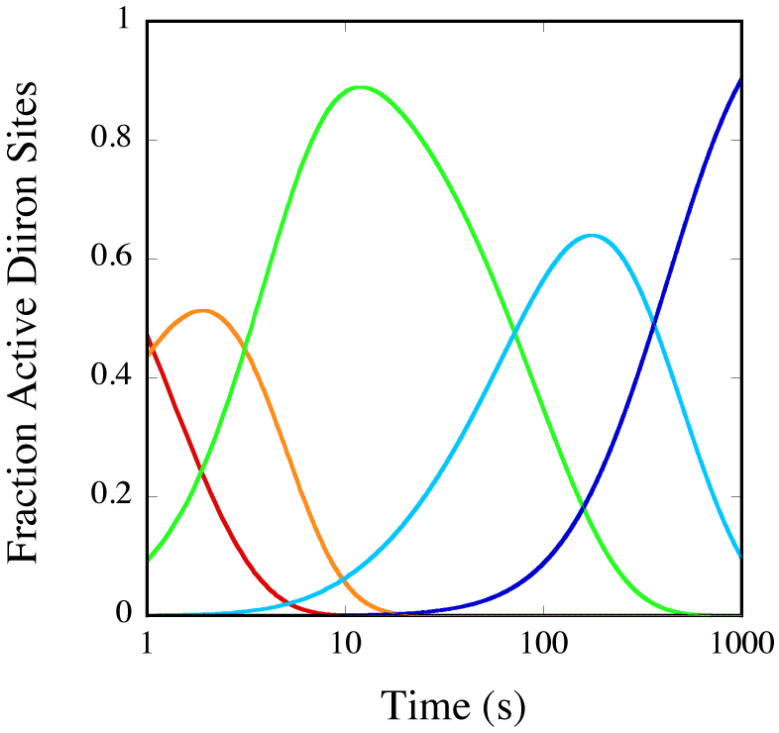

Figure 5.

Speciation plot depicting the time-dependence of transients formed during the reaction of $MMOH_{red}$ with O_2 in the presence of two equiv of MMOB at pH 7.0 and 4 °C. The concentrations of [P^*] (red), [H_{peroxo}] (orange), [Q] (green), [Q^*] (cyan), and [H_{ox}] (blue) as a function of time were calculated from the $P^* \rightarrow H_{peroxo} \rightarrow Q \rightarrow Q^* \rightarrow H_{ox}$ model using rate constants obtained from fits of data to eq 3.

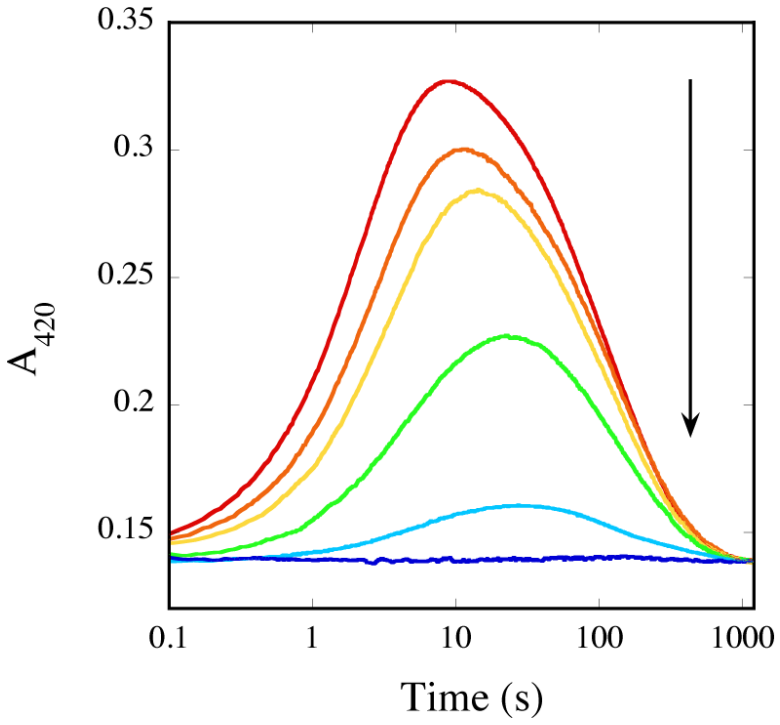

Figure 6.

Representative 420 nm absorbance profiles monitoring the reactions of 50 μM $MMOH_{red}$ with O_2 in the presence of 2 equiv MMOB at 4 °and pH 6.6 (red), pH 7.2 (orange), pH 7.4 (yellow), pH 7.8 (green), pH 8.2 (cyan), and pH 8.6 (blue).

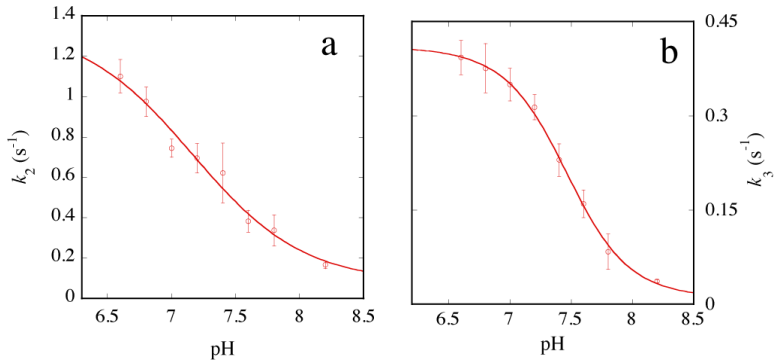

Figure 7.

pH dependencies of P^* decay/H_{peroxo} formation, k_2, (a) and H_{peroxo} decay/Q formation, k_3, (b) at 4 °C. Data were collected and analyzed as noted in the text. Each data point represents the average of 6 or more data sets collected with in the presence (scheme 2i) and absence (scheme 3iii) of 578 μM CH_4 with at least 3 different batches of protein. P^* decay/H_{peroxo} formation data, k_2, (a) fit well to eq 5 describing scheme 5a, whereas those of H_{peroxo} decay/Q formation data, k_3, (b) were fit to eq 6 describing scheme 5b (red lines through points). Error bars depict one standard deviation at the 95% confidence level.

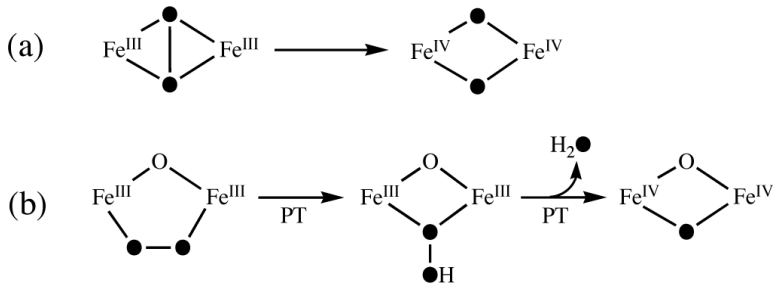

Scheme 1.
Two possible mechanisms of O–O bond cleavage in MMOH.

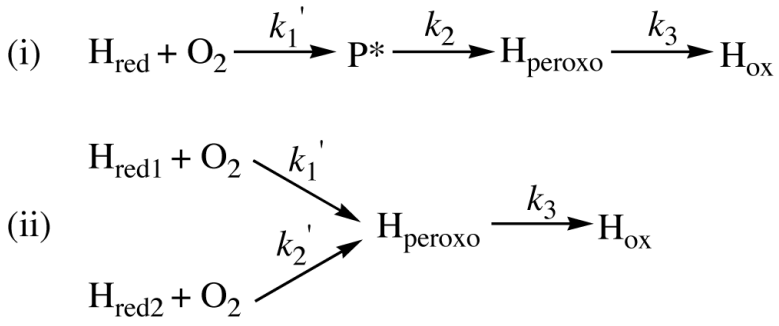

Scheme 2.

Possible models for the reaction of $MMOH_{red}$:2B + O_2 in the presence of 578 μM methane.

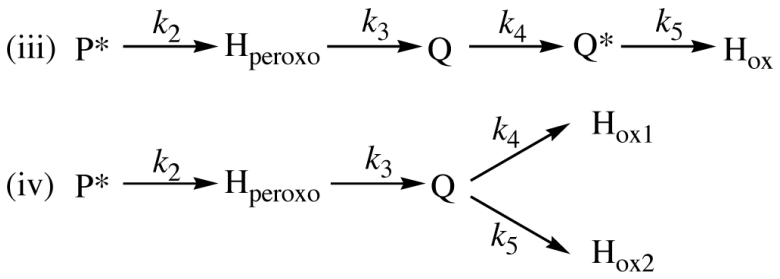

Scheme 3.
Possible models for the reaction of $MMOH_{red}$:2B + O_2.

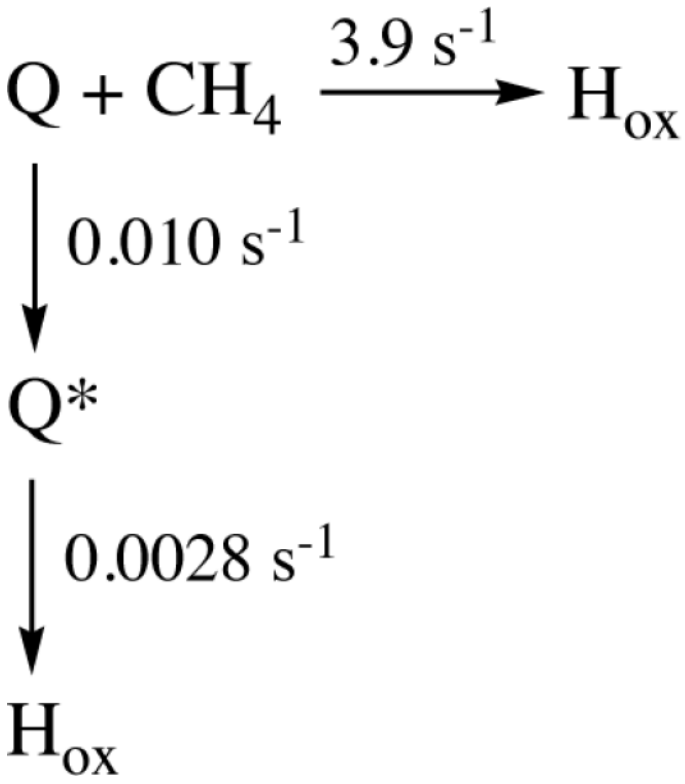

Scheme 4.
Mechanism of Q decay in the presence and absence of 335 μM CH_4.

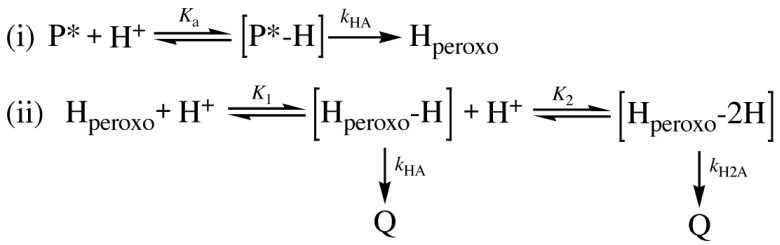

Scheme 5.
Models for the pH dependencies of P^* to H_{peroxo} and H_{peroxo} to Q conversion.

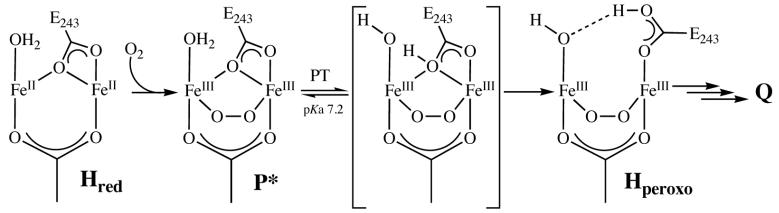

Scheme 6.

One possible mechanism of P^{*} to H_{peroxo} conversion depicting key iron ligands.

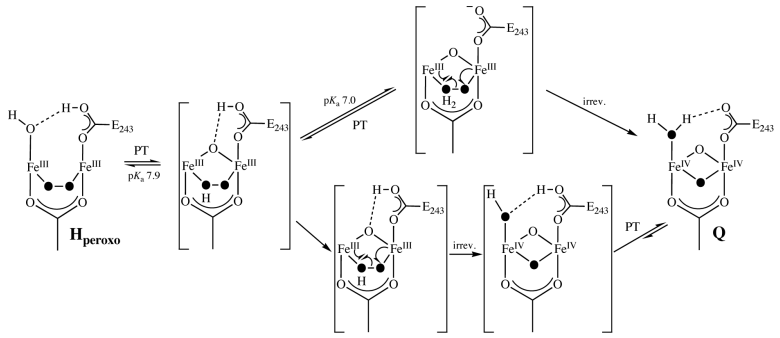

Scheme 7.

One possible mechanism of H_{peroxo} to Q conversion depicting key iron ligands and the oxygen atoms deriving from O_2 in bold.

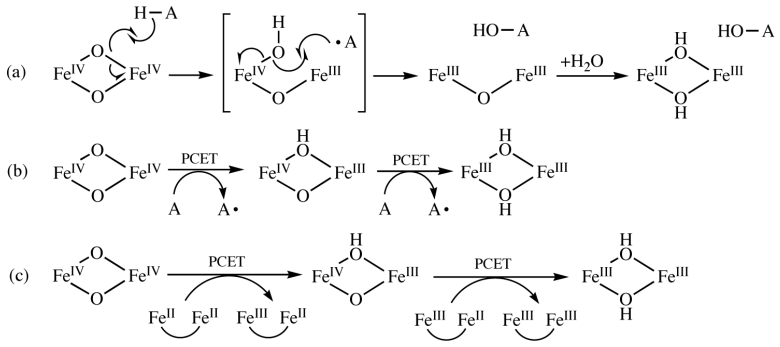

Scheme 8.
Possible mechanisms of Q decay in the absence of hydrocarbon substrates.